FIRST PRINCIPLES STUDY OF STRUCTURAL, ELECTRONIC, AND MECHANICAL PROPERTIES OF LEAD SELENIDE AND LEAD TELLURIDE

THESIS

Presented to the Graduate Council of
Texas State University–San Marcos
in Partial Fulfillment
of the Requirements

for the Degree

Master of SCIENCE

by

John E. Petersen III, B.A., B.S.

San Marcos, TX
May 2013

FIRST PRINCIPLES STUDY OF STRUCTURAL, ELECTRONIC, AND MECHANICAL PROPERTIES OF LEAD SELENIDE AND LEAD TELLURIDE

Committee Members Approved:

_____
Luisa Scolfaro, Chair

_____
Byounghak Lee

_____
Wilhelmus Geerts

Approved:

_____
J. Michael Willoughby
Dean of the Graduate College

FAIR USE AND AUTHOR'S PERMISSION STATEMENT

Fair Use

Duplication Permission

ACKNOWLEDGEMENTS

While all of the work presented here is my own, I would not have been able to accomplish everything without the help of Dr. Luisa Scolfaro. As my advisor, not only did she guide me in research, but she helped me become a better scientist and person. She encouraged me to strive for perfection in all that I did, and I will remember that for the rest of my life. No one could ask for a better mentor. I cannot thank Dr. Byounghak Lee enough for introducing me to her.

She introduced me to some incredible people, as well, including Dr. Wilhemus Geerts, Dr. Thomas Myers, Dr. Thomas Zirkle, and her previous students, Dr. Pablo Borges and Michael Spinks. Dr. Geerts's thought provoking questions helped to fill in some gaps in my knowledge, and I would like to thank him for being on the council. Dr. Myers and Dr. Zirkle were very helpful in answering my questions about experimental methods. Pablo kindly showed me how to utilize the mass streams of data output effectively. Michael inspired me to learn more about Linux, shell scripting, and open source software.

I would not have achieved anything without the encouragement of my family. I would like to thank my mother and father for introducing me to science at a young age.

This manuscript was submitted on March 7, 2013.

TABLE OF CONTENTS

Page

LIST OF TABLES

Table **Page**

LIST OF FIGURES

Figure **Page**

ABSTRACT

FIRST PRINCIPLES STUDY OF STRUCTURAL, ELECTRONIC, AND MECHANICAL PROPERTIES OF LEAD SELENIDE AND LEAD TELLURIDE

by

John E. Petersen III, B.A., B.S.

Texas State University–San Marcos

May 2013

SUPERVISING PROFESSOR: LUISA SCOLFARO

Lead chalcogenides, most notably lead selenide (PbSe) and lead telluride (PbTe), have become an active area of research due to their thermoelectric properties. The high figure of merit (zT) of these materials has brought much attention to them, due to their ability to convert waste heat into electricity. Recent efforts, such as applying pressure or doping, have shown an increase in thermoelectric efficiency. Variation in application and synthesis conditions gives rise to a need for analysis of structural, electronic, and mechanical properties of these materials at different pressures.

In addition to the NaCl structure at ambient conditions, lead chalcogenides have a dynamic orthorhombic (Pnma) intermediate pressure phase and a higher pressure, yet stable, CsCl phase. By altering the lattice constant, the application of external pressure is simulated; this has notable effects on total ground-state energy, band gap, and structural phase.

Using the Projector Augmented Wave (PAW) Method and the Generalized Gradient Approximation (GGA) in Density Functional Theory (DFT), the phase transition pressures are calculated by finding the differences in enthalpy from total energy calculations. For each phase, elastic constants, bulk modulus, shear modulus, and Young's modulus are calculated, and the NaCl phase is studied with typical dopants, both n-type (Bi and I) and p-type (Na, In, and Tl). Pugh's ratio is employed to give insight on the brittleness of the materials and phases studied. In addition to structural and mechanical properties, the band structure and density of states are analyzed at varying pressures, paying special note to thermoelectric implications. The results presented here will be useful to guide future experiments toward the search for structurally stable thermoelectric materials. Several mechanical properties predicted here are ready to be confirmed by experimental works.

CHAPTER 1:

INTRODUCTION

1.1. Motivation

It is well known that the world faces an energy crisis due to dependence on a finite supply of fossil fuels. Not only does the harnessing of energy from fossil fuels have a negative impact on the environment, but much of the energy produced in automobiles, refrigeration, and especially industrial plants is lost in waste heat. Harvesting this waste heat would increase efficiency in power generation, reducing dependence on fossil fuels and ultimately saving money in the process.

Transducing heat into electricity can be achieved by means of thermoelectric materials. These materials have the unique property of having a high electrical conductivity while their thermal conductivity is low. Generally speaking, when the material is exposed to a heat gradient, the electrons (holes) move from the hot (cool) end to the cool (hot) end, creating a potential difference, resulting in an electric field. This process is known as the Seebeck effect. A thermoelectric device can be used to generate electricity by exposing one end to waste heat, while the other end is maintained at ambient conditions.

Efficiency of thermoelectric materials is measured by the figure of merit, a dimensionless quantity, which is

$$zT = \frac{S^2 \sigma T}{\kappa_e + \kappa_l} \quad , \qquad (1.1.1)$$

where σ is the electrical conductivity, T is the temperature, κ_e is the electronic contribution to the thermal conductivity, κ_l is the lattice contribution to the thermal conductivity, and S is the Seebeck coefficient, defined as

$$S = \frac{\boldsymbol{E}}{\nabla T} \qquad (1.1.2)$$

(measured in μV/K), where **E** is the resulting electric field. Unfortunately, thermoelectrics do not yet possess a zT value high enough to be commercially viable [1], [2]. The difficulty lies in the fact that as S increases, σ decreases. Furthermore, an increase in σ leads to an increase in the thermal conductivity as well.

In the 1990's, interest was renewed in thermoelectric possibilities with the advent of nanotechnology. Since then, bulk materials have attracted attention as well, so finding bulk materials with a high zT value has become an active area of research in recent years. Some thermoelectric materials have a higher zT value in different temperature ranges than others. For temperatures up to 475 K, alloys of Bi_2Te_3 and Sb_2Te_3 have been found to be the most efficient for n-type and p-type devices, respectively, with peak zT values being about unity. In the mid-temperature range (500-900 K), group IV-VI materials, such as GeTe and PbTe are commonly studied, with both n-type and p-type dopants and a zT value as high as ~1.5 in thallium doped p-type PbTe at 773 K [2], [3]. At temperatures > 900 K, silicon-germanium alloys, and more recently PbSe, have been found to be the most efficient materials, in both n-type and p-type cases, with a zT value predicted to peak at about 2.0 for hole-doped PbSe at 1000 K [2], [4].

In addition to doping, recent studies have found pressure tuning PbTe increases the power factor œ,

$$œ = S^2 \sigma \quad , \tag{1.1.3}$$

by a factor of ~10 to up to ~170, at pressures between 2 and 3 GPa [5]. Experimentally, pressure is applied by means of a diamond anvil press, exerting quasi-hydrostatic pressure. Here, it is found that varying the lattice constant in ab initio calculations simulates pressure. It has been shown that the band gap of PbTe and PbSe decreases from 0.311 eV and 0.278 eV, respectively, at ambient conditions, to an obscure state with no band gap at ~3 GPa [6]. In highly conductive materials, zT is solely dependent upon S and is determined by

$$zT = \frac{S^2/L}{1+\frac{\kappa_l}{\kappa_e}} \quad , \tag{1.1.4}$$

where $\kappa_l << \kappa_e$, and L is the constant Lorentz factor $2.4 \times 10^{-8}\ J^2K^{-2}C^{-2}$ [2]. Furthermore, the peak in S of PbTe has been found to be at the same pressure (2-2.5 GPa) as the peak in œ [5]; therefore, the enhancement of the power factor cannot be solely due to the increased conductivity.

Another peak in the power factor was found at 6-6.5 GPa. While ambient PbTe and PbSe are found in a rock salt (NaCl) structure, at this pressure, PbTe is in an orthorhombic Pnma phase with a band gap similar to that of ambient PbTe [7]. Since the conductivity remains about the same, while the power factor increases, the Seebeck coefficient must increase, leading to a larger zT value. While now it is clear that PbTe and PbSe have an orthorhombic structure at intermediate pressures [5], [7], the phase was

previously believed to be a GeS structure [8], [9]. PbS, which is not studied as extensively, due to its low potential for thermoelectric applicability, is still believed to have a GeS structure [10]. Since applicability is limited and there appears to be ambiguity about the atomic positions of the intermediate phase, PbS will not be considered in this work. The lead chalcogenides (PbS, PbSe, and PbTe) change phase again at higher pressures to a metallic CsCl phase, which has not only been observed under hydrostatic pressure but has also been grown on substrate [11], [12]. The thermoelectric applicability of this phase is not yet clear.

By means of ab initio (first principles) calculations, this work will investigate the general structural properties, electronic properties, and structural phase transition pressures of lead chalcogenides, but thermoelectric properties will not be considered explicitly. Since synthesizing under pressure, doping, and exposure to heat can all cause mechanical stress to the materials, it is important to understand their resiliency, if they are to be used commercially. Ductility is particularly important for commercial use, so mechanical properties are calculated for the three phases of PbSe and PbTe, and analysis is carried out to predict the ductile or brittle behavior of the materials. For the NaCl phase, both the intrinsic materials and doped versions are considered, where Na, In, and Tl (p-type) and I and Bi (n-type) are the impurities studied. All results are compared with available experimental and theoretical findings of other works.

1.2 Crystalline Structure of Lead Chalcogenides and their Brillouin Zones

Before looking at the theory behind ab initio calculations and the computational package used in this work, it is necessary to look at the atomic structures of the materials under question. From the atomic positions, as will be revealed in Sections 2.1 and 2.2, the total ground-state energy of the system can be calculated, which is paramount to all first principles calculations and analysis. It must be noted that perfect crystalline lattice structures are assumed in all calculations of this work. This means that the systems calculated have atoms that form a basis structure, or unit cell, that is repeated periodically in the x, y, and z directions according to the length of the lattice vectors (**a**, **b**, and **c**, respectively). According to the Bloch Theorem, only a unit cell is necessary to calculate eigenvalues and total energy of a finite crystalline structure [13]. The theorem states:

$$\varphi_{nk}(\boldsymbol{r}) = e^{i\boldsymbol{k}\cdot\boldsymbol{r}} u_{nk}(\boldsymbol{r}) \quad , \qquad (1.2.1)$$

where φ is the one-orbital wave function (see Equation 2.2.15) for a band in the band structure, n is the number of the band or orbital in question (equivalent to the i in Equation 2.2.15), **k** is the wave vector for that band, and u is the periodic Bloch function that has the same period as the potential energy throughout the crystal. Since it is periodic with each unit cell, the wave function is also the same in each unit cell; therefore, the Hamiltonian is also periodic with **r** and the same for each unit cell, where $\mathbf{r} = \mathbf{r} + \mathbf{a}_i$ (with $\mathbf{a}_i$ being a unit vector and i corresponding to a 1, 2, or 3 in Equations 1.1.2 and 1.2.3). Thus, from only the atomic positions in the unit cell, the number of electrons, and the charge of the nuclei, the total energy of the system (of finite unit cells) can be calculated by solving the many-body problem (Section 2.1).

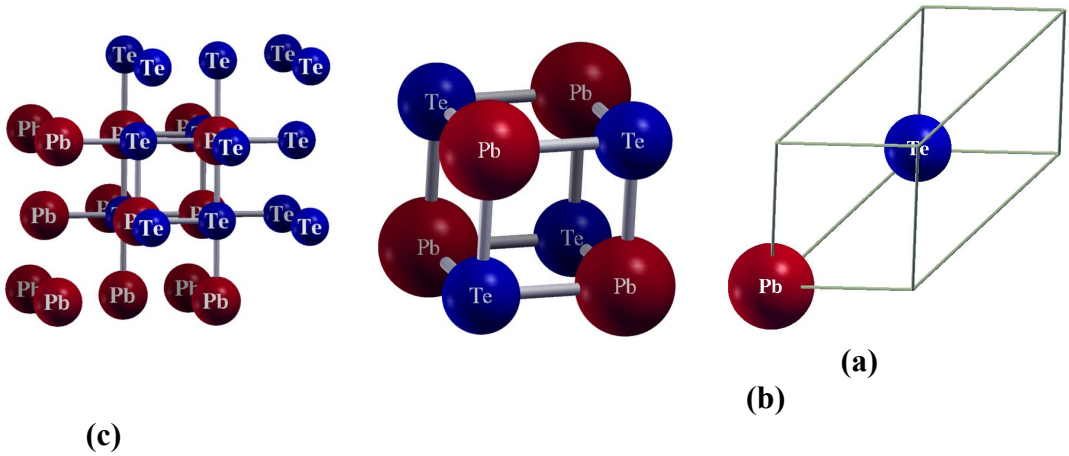

Figure 1.2.1. NaCl Structure and Primitive Cell. ***(a)*** *contains one FCC cell for each ion, in order to visualize how they are interlaced. It is not to be considered a unit cell. Bonds are indicated by grey bars.* ***(b)*** *is an eight ion cubic unit cell.* ***(c)*** *is the primitive FCC two-ionic-type unit cell. While the FCC symmetry remains, this primitive cell is of the triclinic shape, outlined in grey in order to assist the reader in seeing the ionic orientation. The Tellurium is in the center of the triclinic cell. The Pb and Te atoms in this cell correspond to those of opposite corners in 1.2.1b. Here, original models were produced by XCrysden software [14].*

The NaCl structure – which is how lead chalcogenides exist in ambient conditions – have two interlaced face-centered cubic (FCC) structures. This means that each cation and anion form a cube with the respective ion positioned at each face of the cube. Since the two FCC structures are interlaced, the opposite ion is positioned half-way in between the second nearest neighbors of the same ion type. The cation and anion could be replaced, and the structure would be exactly the same. See Figure 1.2.1a. Thus, a simple cubic unit cell can be modeled with eight ions total (Figure 1.2.1b). The lattice vectors in this case would be of the simple cubic form, with equal magnitudes:

$$\boldsymbol{a}_1 = a\,\boldsymbol{i}$$

$$\boldsymbol{a}_2 = a\,\boldsymbol{j} \qquad (1.2.2)$$

$$\boldsymbol{a}_2 = a\,\boldsymbol{k} \quad ,$$

where **i**, **j**, and **k** are unit vectors in the x, y, and z directions, respectively. This unit cell can be reduced to the FCC primitive cell (Figure 1.2.1c), which has a basis of two atoms with the following lattice vectors:

$$\boldsymbol{a}_1 = \frac{a}{2}(\boldsymbol{i}+\boldsymbol{j})$$

$$\boldsymbol{a}_2 = \frac{a}{2}(\boldsymbol{i}+\boldsymbol{k}) \qquad (1.2.3)$$

$$\boldsymbol{a}_3 = \frac{a}{2}(\boldsymbol{j}+\boldsymbol{k}) \quad .$$

The two above models of the NaCl structure produce the exact same crystalline structure; however, the periodicities correspond to the respective lattice vectors [13]. For PbSe, a = 6.124 Å, and for PbTe, a = 6.462 Å [1].

As mentioned in the previous section, when pressure is applied to PbSe or PbTe, structural phase transitions occur. The intermediate phase is an orthorhombic Pnma structure with independent directionally orthogonal lattice constants, i.e. $|\mathbf{a}_1| \neq |\mathbf{a}_2| \neq |\mathbf{a}_3|$. Lattice constants and ionic positions have been measured experimentally [15], [16], and will be compared to this work's calculated values in a following section. In Figure 1.2.2a, one can see an overview of the Pnma structure of PbTe, while Figure 1.2.2b shows the primitive cell. The higher pressure phase is a CsCl phase, or an interlaced two-ion-type simple cubic (SC) phase, where the lattice constants

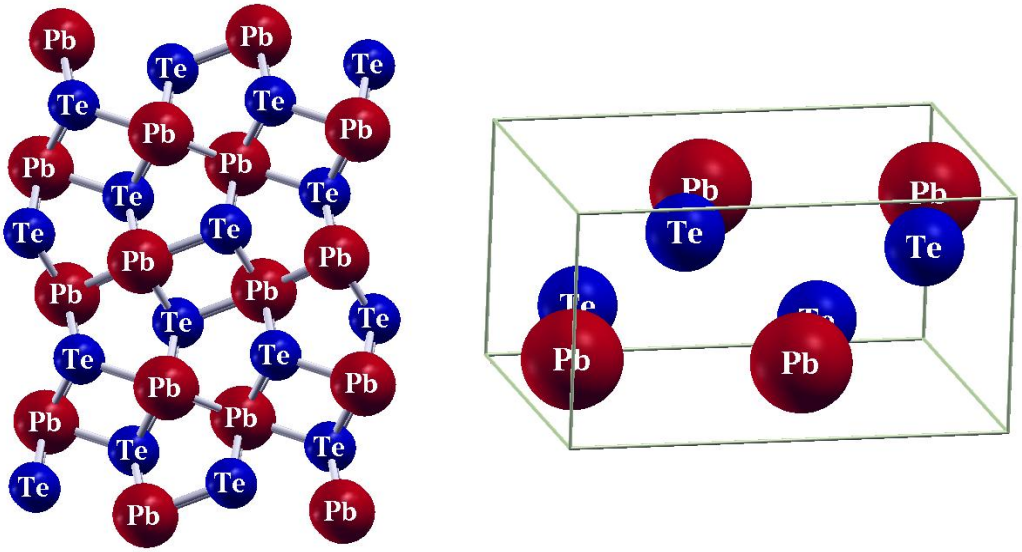

Figure 1.2.2. Pnma Crystal Structure and Primitive Cell. ***(a)*** *shows an overview of the Pnma structure of PbTe.* ***(b)**** *shows the primitive cell used in the calculations of this work. The above images were produced using XCrysden [14].*

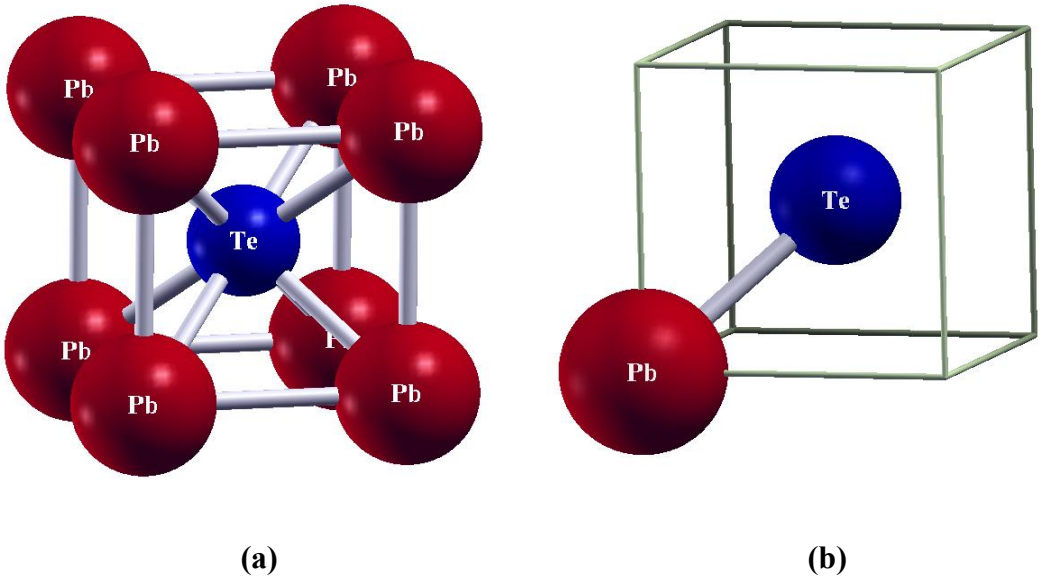

Figure 1.2.3. CsCl Crystal Structure and Primitive Cell. ***(a)*** *shows an overview of the CsCl structure of PbSe and PbTe.* ***(b)*** *shows the primitive cell used in the calculations of this work. The SC cell shape is outlined in grey in order to assist the reader in seeing the ionic orientation. Again, Xcrysden was used to produce the images [14].*

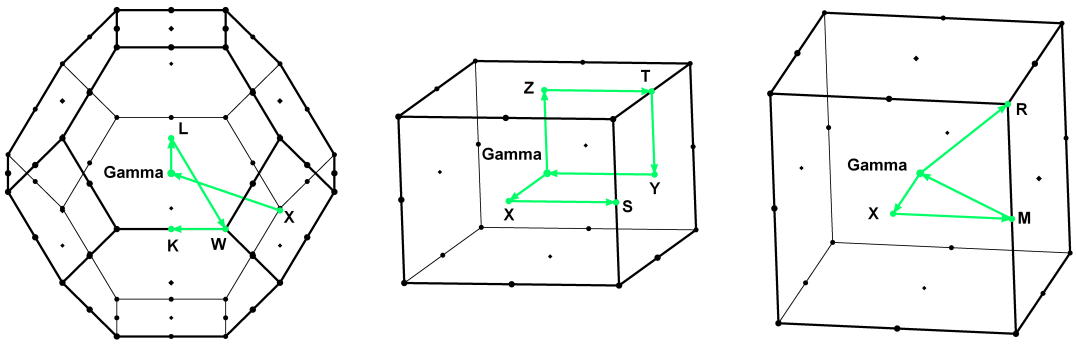

(a) **(b)** **(c)**

Figure 1.2.4. Brillouin Zones of the Three Structures. *The Brillouin zones and paths of* ***(a)*** *the NaCl structure,* ***(b)*** *the orthorhombic structure (Pnma), and* ***(c)*** *the CsCl Structure. Images generated by XCrysden [14].*

$|\mathbf{a}_1| = |\mathbf{a}_2| = |\mathbf{a}_3|$ are directionally orthogonal. Figure 1.2.3a shows the overall CsCl structure of PbSe and PbTe, while Figure 1.2.3b shows the primitive cell.

The first Brillouin zone of the ambient FCC (NaCl or rock salt) structural phase of PbSe and PbTe is a body-centered cubic (BCC) cell, which is also the Wigner-Seitz cell (however, if the unit cell of Equation 1.2.2 and Figure 1.2.1b is used, the Brillouin zone is simple cubic). It has the shape of a truncated octahedron. The path traced through the cell when calculating the band structure is $X \rightarrow \Gamma \rightarrow L \rightarrow W \rightarrow K$ (Figure 1.2.4a). The intermediate pressure orthorhombic (Pnma) phase has an orthorhombic Brillouin zone, with a path traced through $\Gamma \rightarrow Z \rightarrow T \rightarrow Y \rightarrow \Gamma \rightarrow X \rightarrow S$ (Figure 1.2.4b). The high pressure CsCl (SC) phase has an SC Brillouin zone, with a path traced through $\Gamma \rightarrow X \rightarrow M \rightarrow \Gamma \rightarrow R$ (Figure 1.2.4c) [13], [17].

CHAPTER 2:

THEORETICAL FUNDAMENTALS OF AB INITIO CALCULATIONS AND THE COMPUTATIONAL PACKAGE VASP

2.1 The Many-Body Problem

The positions of the nuclei and electrons and the forces and energies between them are crucial in the calculations of this work. While energy is an important concept in all branches of physics, it will be evident in Chapter 3 that many properties can be calculated from the total energy of a system. Before one can derive other quantities, however, one must understand how to calculate the total energy of a system in the first place. It is tempting to model the system of particles using classical means; however, since the system is evaluated at such a small scale, it is known that quantum constructs are necessary to model the system with any accuracy. Nevertheless, it is helpful to review the classical picture of the N-body problem before the quantum mechanical many-body problem.

Assuming a stationary system – or, more specifically, a system of particles which are in an inertial reference frame – the total energy can be calculated as follows:

$$E = T + V \quad , \tag{2.1.1}$$

where T is the total kinetic energy of the system:

$$T = \frac{1}{2}\sum_i m_i v_i^2 \quad ; \tag{2.1.2}$$

and, V is the sum of the potential energies between all particles:

$$V = \sum_i V_i + \frac{1}{2}\sum_{i \neq j} V_{ij} \quad , \qquad (2.1.3)$$

where the first term on the right is the external potential energy, and V_{ij} corresponds to the potential energy between the i^{th} and j^{th} particle; the ½ is so that forces between two particles in the summation are not counted twice. In the systems considered in this work, external potential energy will be ignored, due to an absence of external fields, so the classical picture of the total energy [18] is

$$E = \frac{1}{2}\sum_i m_i v_i^2 + \frac{1}{2}\sum_{i \neq j} V_{ij} \quad . \qquad (2.1.4)$$

The potential energy between two point particles is purely Coulombic in this case, and the total energy becomes [19] (Hartree atomic units will be used throughout this work)

$$E = \frac{1}{2}\sum_i m_i v_i^2 + \frac{1}{2}\sum_{i \neq j} \frac{q_i q_j}{|r_i - r_j|} \quad . \qquad (2.1.5)$$

Since calculations are performed at the quantum level in this study, the N-body problem is insufficient to describe the system. The electrons interact via Coulomb two-body forces, yet they are not localized and are represented by a wave function. Thus, quantum mechanical operators are used in the many-body problem as the basis for calculating the total energy of a system of nuclei and electrons. A system of atoms, which are in a unit cell of a crystal lattice, all have energies which must be summed together in order to get the total ground-state energy. The electrons are mobile, and have kinetic energy, while the ions are more or less stationary. Furthermore, the masses of the nuclei are much larger than the mass of an electron, so the Born-Oppenheimer approximation

will be used, and the kinetic energy of the nuclei will be ignored. This approximation breaks the sum of the potential energies into constituent parts, as will be shown below.

Throughout the rest of this work, Dirac's bra-ket notation will be used [20], [21], where for a given operator $\hat{A}$ and time independent N-electron ground state wave function $\boldsymbol{\Phi}$,

$$\langle \boldsymbol{\Phi} | \hat{A} | \boldsymbol{\Phi} \rangle = \int \boldsymbol{\Phi}^{*}(\boldsymbol{r}) \hat{A} \boldsymbol{\Phi}(\boldsymbol{r}) \, d\boldsymbol{r} \quad . \tag{2.1.6}$$

The Schrödinger Equation can be written in this notation, with the Hamiltonian and the total ground state energy for an N-electron unit cell (Section 3.2) in the absence of an external field (a pure Coulomb system):

$$\langle \boldsymbol{\Phi} | \hat{\boldsymbol{H}} | \boldsymbol{\Phi} \rangle = \langle \boldsymbol{\Phi} | \left(\hat{\boldsymbol{T}} + \hat{V}_{ne} + \hat{\boldsymbol{U}}_{ee} \right) | \boldsymbol{\Phi} \rangle + U_{nn} = \mathrm{E} \quad , \tag{2.1.7}$$

where U_{nn} is classical in the Born-Oppenheimer approximation and thus not a quantum mechanical operator. The total kinetic energy of the electrons is

$$\hat{\boldsymbol{T}} = -\frac{1}{2} \sum_{i=1}^{N} \nabla_i^2 \quad . \tag{2.1.8}$$

The nucleus-electron potentials sum to

$$\hat{V}_{ne} = -\sum_{i,j} \frac{Z_i}{|\boldsymbol{r}_i - \boldsymbol{r}_j|} \quad , \tag{2.1.9}$$

where the negative sign indicates an attractive potential, Z_i corresponds to the charge of the nucleus at position $\mathbf{r}_i$, and $\mathbf{r}_j$ is the position of each electron. The electron-electron interaction is described by

$$\hat{\boldsymbol{U}}_{ee} = \frac{1}{2} \sum_{i \neq j} \frac{1}{|\boldsymbol{r}_i - \boldsymbol{r}_j|} \quad . \tag{2.1.10}$$

The nucleus-nucleus interaction is

$$U_{nn}=\frac{1}{2}\sum_{i\neq j}\frac{Z_i Z_j}{|\boldsymbol{r}_i-\boldsymbol{r}_j|} \quad , \tag{2.1.11}$$

where the i and j scripts should not be confused with the previous cases. If Equation 2.1.7 were written out explicitly, indices would need to be adjusted accordingly. The nucleus-nucleus potential in Equation 2.1.11 is classical, yet essential in the total energy calculation; nevertheless, it is frequently omitted when discussing the total energy. The nucleus-electron interaction in Equation 2.1.9 can be written in terms of particle density, which is fundamental to electronic structure theory:

$$\hat{n}(\boldsymbol{r})=\sum_{i=1}^{N}\delta(\boldsymbol{r}-\boldsymbol{r}_i) \quad ; \tag{2.1.12}$$

$$n(\boldsymbol{r})=\frac{\langle\boldsymbol{\Phi}|\hat{n}(\boldsymbol{r})|\boldsymbol{\Phi}\rangle}{\langle\boldsymbol{\Phi}\|\boldsymbol{\Phi}\rangle} \quad ; \tag{2.1.13}$$

$$V_{ne}=\frac{\langle\boldsymbol{\Phi}|\hat{V}_{ne}|\boldsymbol{\Phi}\rangle}{\langle\boldsymbol{\Phi}\|\boldsymbol{\Phi}\rangle}=\int\hat{V}_{ne}\,n(\boldsymbol{r})\,d^3\boldsymbol{r} \quad . \tag{2.1.14}$$

2.2 Density Functional Theory

As can be seen from 2.1.12-14, the electronic density is the fundamental variable of the many-body problem. This was proposed by Thomas and Fermi at about the same time as Hartree (1927-1928) [21]. Without resorting to approximations, Schrödinger's equation can only be solved for simple systems. Thomas and Fermi based their approximations on the Drude model, which treats electrons as a homogeneous gas. Unfortunately, the model of Thomas and Fermi was too crude to be of much use, since it neglects exchange and correlation (Section 2.2.2 and 2.2.3). However, it was the basis for

the Kohn-Sham self-consistent equations, which are the foundation for modern Density Functional Theory (DFT). Before looking at the Kohn-Sham equations, however, it is necessary to state the Hohenberg-Kohn theorems which illustrate the importance of electron density.

2.2.1 Hohenberg-Kohn Theorems

The first theorem proves by Rayleigh-Ritz's variational principle that V_{ne} is determined solely by n(**r**) [22]. Furthermore, there is only one value for n(**r**) and one value for V_{ne} that corresponds to the electronic density and nucleus-electron potential energy of the ground state. In the context of DFT, n(**r**) refers specifically to the electron density of the ground state. Since the ground state N-particle wave function **Φ** depends explicitly on V_{ne} (Equation 2.1.7), it also depends on n(**r**), and **Φ** can be found by solving the full many-body Schrödinger equation. Then, the ground state energy can be found from Equation 2.1.7.

The second theorem proves, by Rayleigh-Ritz, that for any ñ(**r**) ≠ n(**r**) [22],

$$E_0 = E_v[n(\boldsymbol{r})] < E_v[\tilde{n}(\boldsymbol{r})] \quad ; \tag{2.2.1}$$

where

$$E_v[n(\boldsymbol{r})] = F[n(\boldsymbol{r})] + \int \hat{\boldsymbol{V}}_{ne}\, n(\boldsymbol{r})\, d^3\boldsymbol{r} + U_{nn} \quad , \tag{2.2.2}$$

and

$$F[n(\boldsymbol{r})] = \langle \boldsymbol{\Phi}[n(\boldsymbol{r})] \left| \hat{\boldsymbol{T}} + \hat{\boldsymbol{U}}_{ee} \right| \boldsymbol{\Phi}[n(\boldsymbol{r})] \rangle \quad . \tag{2.2.3}$$

Equations 2.2.1-3 require that E_v be a variational functional dependent solely upon the electron density function. Therefore, the ground state energy E_0 corresponds to the energy

of the system with the specific ground state electron density n(**r**) [21]. These are the fundamental mathematical theorems of DFT.

2.2.2 The Kohn-Sham Self-Consistent Equations

It was shown in Section 2.1 how the Hamiltonian of the quantum mechanical many-body problem was split up into multiple components to account for the differences in mathematical operators involved in calculating the energies in a Coulombic system at small scale. In Kohn-Sham theory, one such component, the electron-electron potential U_{ee}, must be broken up further in order to account for exchange and correlation. Correlation corresponds to a potential energy term that takes into account the probability that an electron at position **r** has a low chance of being close to another electron at **r'** – with n(**r**) and n(**r'**) being in a dual space within the same volume – and a high chance of being farther away, due to the Coulomb repulsion. Here, this probability will be represented as g(**r**, **r'**). Due to the wavelike nature of electrons, g(**r**, **r'**) for correlation is not simple to calculate and is only known for homogeneous systems. Exchange, on the other hand, can be calculated very precisely. Exchange arises from the Pauli Exclusion Principle, which states that electrons of the same spin cannot occupy the same position (orbital); however, an electron of opposite spin can. Therefore, taking only exchange into account leads to a g(**r**, **r'**) which approaches ½ as **r** approaches **r'**.

The full electron-electron potential U_{ee} can now be written [21] as

$$U_{ee}=\frac{1}{2}\int\int\frac{n(\boldsymbol{r})n(\boldsymbol{r}')}{|\boldsymbol{r}-\boldsymbol{r}'|}d^3\boldsymbol{r}\,d^3\boldsymbol{r}'+\frac{1}{2}\int\int\frac{n(\boldsymbol{r})n(\boldsymbol{r}')}{|\boldsymbol{r}-\boldsymbol{r}'|}[g(\boldsymbol{r},\boldsymbol{r}')-1]d^3\boldsymbol{r}\,d^3\boldsymbol{r}' \quad , \qquad (2.2.4)$$

where the first term on the right-hand side is known as the Hartree potential, which is

classical and electrostatic, and the second term on the right-hand side is the combined exchange and correlation correction from quantum mechanics, which includes the probability g(**r**, **r'**). The Hartree potential is the largest contribution to U_{ee} and known exactly, followed by the exchange, which can also be calculated precisely, and the smallest contribution is the correlation, which must be approximated. Approximation methods for exchange and correlation will be discussed further in section 2.2.3, but the Kohn-Sham approach will be covered here. Their approximation, as is customarily done in modern approximations, combines exchange and correlation into one functional. They assert [23] that since the exchange and correlation energy ε_{xc} of a single electron in a homogeneous electron gas is known, assuming homogeneity of electron density in more complicated systems leads to the equation:

$$E_{XC} = \int n(\boldsymbol{r}) \epsilon_{XC}[n(\boldsymbol{r})] d^3\boldsymbol{r} \quad . \qquad (2.2.5)$$

Electron-electron interactions such as exchange and correlation directly affect the kinetic energy; furthermore, the many-body problem does not take electron orbitals into account. Since the key variable in the many-body problem is the electronic density, Kohn and Sham's idea was to find a system of non-interacting electrons which had the same electronic density as that of the interacting system and treat it as homogeneous. Once the non-interacting density is exactly the same as the interacting one, the chemical potential μ will be the same in both cases; otherwise, charge would flow from one to the other, if they were adjacent. Assuming the occupation number of each orbital φ is 2, the density of the non-interacting or reference system $n_R(\mathbf{r})$ can be found by

$$n_R(\boldsymbol{r}) = 2\sum_{i=1}^{N_\varphi} |\varphi_i(\boldsymbol{r})|^2 \quad , \tag{2.2.6}$$

where N_φ is the number of orbitals in the volume considered ($N_\varphi = N/2$ for a closed-orbital system). Then, the kinetic energy of this reference system $T_R[n(\mathbf{r})]$ (not to be confused with the trace of a matrix) could be calculated exactly:

$$T_R[n_R(\boldsymbol{r})] = -\sum_{i=1}^{N_\varphi} \langle \varphi_i | \nabla^2 | \varphi_i \rangle \quad . \tag{2.2.7}$$

In open-shell systems, the number of spin up electrons is not the same as the number of spin down electrons, and spin density needs to be taken into account:

$$T_R[n_{\uparrow_R}(\boldsymbol{r}), n_{\downarrow_R}(\boldsymbol{r})] = -\frac{1}{2}\sum_{\sigma=1}^{2}\sum_{i=1}^{N_\varphi} \langle \varphi_{i,\sigma} | \nabla^2 | \varphi_{i,\sigma} \rangle \quad . \tag{2.2.8}$$

Ignoring spin density, the full Kohn-Sham ground-state energy equation becomes [20], [21], [23]

$$\begin{aligned} E = &-\sum_{i=1}^{N_\varphi} \langle \varphi_i | \nabla^2 | \varphi_i \rangle - \sum_{j=1}^{P} \int \frac{Z_j n_R(\boldsymbol{r})}{|\boldsymbol{r}_j - \boldsymbol{r}|} d^3\boldsymbol{r} + \frac{1}{2}\sum_{j\neq k} \frac{Z_j Z_k}{|\boldsymbol{r}_j - \boldsymbol{r}_k|} \quad ; \\ &+ \frac{1}{2}\int\int \frac{n_R(\boldsymbol{r}) n_R(\boldsymbol{r}')}{|\boldsymbol{r} - \boldsymbol{r}'|} d^3\boldsymbol{r}\, d^3\boldsymbol{r}' + \int n_R(\boldsymbol{r}) \epsilon_{XC}[n_R(\boldsymbol{r})] d^3\boldsymbol{r} \end{aligned} \tag{2.2.9}$$

or, more simply,

$$E - U_{nn} = T_R[n_R(\boldsymbol{r})] + \int \hat{\boldsymbol{V}}_{ne} n_R(\boldsymbol{r}) d^3\boldsymbol{r} + \int n_R(\boldsymbol{r}) \hat{\boldsymbol{U}}_{ee} n_R(\boldsymbol{r}') d^3\boldsymbol{r} + E_{XC} \quad , \tag{2.2.10}$$

where $\hat{\boldsymbol{V}}_{ne}$, $\hat{\boldsymbol{U}}_{ee}$, and U_{nn} correspond to equations 2.1.9, 2.1.10, and 2.1.11 respectively. To obtain that energy, however, a series of self-consistent equations [23] must take an initial approximate $n_R(\mathbf{r})$ to iteratively calculate a more accurate $n_R(\mathbf{r})$ and E. Applying the variational principle to the total ground-state energy, subject to the condition

$$\int \delta n_R(\boldsymbol{r})\, d^3\boldsymbol{r} = 0 \quad , \tag{2.2.11}$$

one obtains

$$\int [\delta n_R(\boldsymbol{r})]\{\hat{V}_{ne} + \int \hat{U}_{ee}\, n_R(\boldsymbol{r}')\, d^3\boldsymbol{r}' + \frac{\delta T_R[n_R(\boldsymbol{r})]}{\delta n_R(\boldsymbol{r})} + \mu_{XC}[n_R(\boldsymbol{r})]\}\, d^3\boldsymbol{r} \quad , \tag{2.2.12}$$

where μ_{XC} is the exchange and correlation contribution to the chemical potential from the homogeneous electron gas of density n_R. The first step in the iterative process is to calculate

$$\hat{V}_{ne} + \int \hat{U}_{ee}\, n_R(\boldsymbol{r}')\, d^3\boldsymbol{r}' \tag{2.2.13}$$

from the presumed homogeneous n_R. Then, μ_{XC} is calculated from

$$\mu_{XC}[n(\boldsymbol{r})] = \frac{\delta E_{XC}}{\delta n_R(\boldsymbol{r})} = \epsilon_{XC}[n_R(\boldsymbol{r})] + n_R(\boldsymbol{r}) \frac{\partial \epsilon_{XC}[n_R(\boldsymbol{r})]}{\partial n_R(\boldsymbol{r})} \quad . \tag{2.2.14}$$

The values from 2.2.13 and 2.2.14 are then substituted into equation 2.2.12, so that eigenvalues ε_i and eigenvector wave functions $\boldsymbol{\varphi}_i$ can be found from the set of one-orbital Schrödinger equations:

$$\{-\frac{1}{2}\nabla^2 + \hat{V}_{ne} + \int \hat{U}_{ee}\, n_R(\boldsymbol{r}')\, d^3\boldsymbol{r}' + \mu_{XC}[n_R(\boldsymbol{r})]\}\, \boldsymbol{\varphi}_i[n_R(\boldsymbol{r})] = \epsilon_i\, \boldsymbol{\varphi}_i[n_R(\boldsymbol{r})] \quad . \tag{2.2.15}$$

A new charge density, $n_{Rout}(\mathbf{r})$, that is no longer homogeneous and changes with $\mathbf{r}$, can be calculated by:

$$n_{R_{out}}(\boldsymbol{r}) = 2 \sum_{i=1}^{N_\varphi} |\boldsymbol{\varphi}_i|^2 \quad . \tag{2.2.16}$$

The process can be repeated iteratively, achieving a more and more accurate electron density (accurate up to ∇^4), until the desired accuracy for E and the eigenvalues ε_i is obtained. The computational software Vienna Ab Initio Simulation Package (VASP) [24],

[25], which is used for all ground-state energy and eigenvalue calculations in this work, is based on these fundamental self-consistent equations (2.2.13-16) of Kohn-Sham theory. The importance of the ground-state energy E will be evident throughout the rest of this work. Since the final converged electron density changes with **r**, it also changes with **k** (the reciprocal lattice position vector, briefly discussed in section 1.2), resulting in unique eigenvalues ε_i for each valence electron at each k point, which are calculated from 2.2.15.

2.2.3 Exchange and Correlation Approximations

Many approximations exist for calculating exchange and correlation, from the Local Density Approximation (LDA) introduced by Kohn and Sham to more modern and complicated methods, such as the hybrid functional. Here, only LDA, the Generalized Gradient Approximation (GGA), and the hybrid functional (HSE) will be considered, since they are the focus of this work. As mentioned in the previous section, the approximation for exchange and correlation is composed of one term, E_{XC} (the second term on the right-hand side of Equation 2.2.4). Since an electron at **r** dramatically reduces the probability of having another electron at **r'** being in the vicinity of **r**, there is a fictitious charge depletion about **r**, known as the exchange-correlation hole (XC hole), represented [21] by

$$n_{XC}(\boldsymbol{r},\boldsymbol{r}')=n(\boldsymbol{r}')[g(\boldsymbol{r},\boldsymbol{r}')-1] \quad . \tag{2.2.17}$$

The XC hole density n_{XC} is non-local, symmetric under exchange of **r** and **r'**, and contains exactly one displaced electron or hole:

$$\int n_{XC}(\boldsymbol{r},\boldsymbol{r}')\,d\boldsymbol{r}'=-1 \quad . \tag{2.2.18}$$

In LDA, while the electron density is local, the XC hole is non-local and defined by

$$n_{XC}^{LDA}(\boldsymbol{r},\boldsymbol{r}')=n(\boldsymbol{r})\{g[|\boldsymbol{r}-\boldsymbol{r}'|,n(\boldsymbol{r})]-1\} \quad . \tag{2.2.19}$$

Since $n(\boldsymbol{r})$ is homogeneous, the pair-correlation function $g[|\boldsymbol{r}-\boldsymbol{r}'|, n(\boldsymbol{r})]$ depends only on the distance between $\boldsymbol{r}$ and $\boldsymbol{r}'$. The exchange part of g, g_X, is known exactly for a homogeneous electron gas, and is given by

$$g_X(\boldsymbol{r},\boldsymbol{r}')=1-\sum_{s=1}^{2}\frac{|n_s(\boldsymbol{r},\boldsymbol{r}')|^2}{n(\boldsymbol{r})n(\boldsymbol{r}')} \quad , \tag{2.2.20}$$

where the s indicates that the sum runs over the two spin projections. By numerical methods, g_C can be solved for exactly, as well [26], and $g = g_X + g_C$. The approximation in LDA is that the initial n(**r**) in the self-consistent calculation is homogeneous. The exchange-correlation energy is calculated by

$$E_{XC}^{LDA}[n(\boldsymbol{r})]=\int n(\boldsymbol{r})\epsilon_{XC}^{LDA}[n(\boldsymbol{r})]d\boldsymbol{r}^3 \quad , \tag{2.2.21}$$

where epsilon is the LDA exchange and correlation energy density:

$$\epsilon_{XC}^{LDA}[n(\boldsymbol{r})]=\frac{1}{2}\int\frac{n_{XC}^{LDA}(\boldsymbol{r},\boldsymbol{r}')}{|\boldsymbol{r}-\boldsymbol{r}'|}d\boldsymbol{r}' \quad . \tag{2.2.22}$$

LDA is very successful at approximating total ground-state energy and eigenvalues in systems where the electron density is very uniform, such as in metals. However, a more accurate picture for more complex systems can be obtained by GGA. Rather than treating the initial electron density as homogeneous, GGA uses a gradient approximation that assumes a more concentrated electron density for values of **r** which are closer to the nuclei. This is achieved by carrying out an expansion of the electron

density in terms of the gradient and higher derivatives. Thus, GGA improves total energy calculations over LDA (in most cases) by expanding and softening bonds [27], [28]. However, sometimes energies are over-corrected [29]. GGA works best in systems of density inhomogeneity [27], [28]. In GGA, the exchange-correlation energy can be written [21] as

$$E_{XC}[n(\boldsymbol{r})]=\int n(\boldsymbol{r})\epsilon_{XC}^{LDA}[n(\boldsymbol{r})]F_{XC}[n(\boldsymbol{r}),\nabla n(\boldsymbol{r}),\nabla^2 n(\boldsymbol{r}),...]d^3\boldsymbol{r} \quad ; \qquad (2.2.23)$$

or, more explicitly

$$E_{XC}[n(\boldsymbol{r})]=\int\{A_{XC}[n(\boldsymbol{r})]\}[n(\boldsymbol{r})]^{4/3}d^3\boldsymbol{r}+\int\frac{\{C_{XC}[n(\boldsymbol{r})]\}|\nabla n(\boldsymbol{r})|^2}{[n(\boldsymbol{r})]^{4/3}}d^3\boldsymbol{r} \quad , \quad (2.2.24)$$

where F_{XC} is the gradient expansion correction functional, and A_{XC} and C_{XC} are first and third order coefficients of the expansion, respectively. In the case of LDA, F_{XC} is equal to one.

In the early years of GGA, it was found that the first order correction actually worsens the LDA calculation of the correlation energy [21], [30]. This problem was rectified by Langreth and Mehl in 1981 [21], [31]; however, problems remained with the exchange energy. When modifying the LDA exchange-correlation density by means of F_{XC}, the condition of 2.2.18 – that the electron hole normalizes to negative one – is violated. Perdew showed in 1985 [32] that imposing this condition upon the functional F_{XC} improves the approximation of the exchange energy dramatically. Numerous GGA methods were produced in the literature, and in 1996, the method of Perdew, Burke, and Erzenhof (PBE) [27], [28] was introduced, which improved the approximation for exchange and correlation energies. The PBE functional gives

$$E_C^{GGA}[n_\uparrow(\boldsymbol{r}), n_\downarrow(\boldsymbol{r})] = \int n(\boldsymbol{r})[E_C^{LDA}(r_s, \zeta) + H(r_s, \zeta, t)]d^3\boldsymbol{r} \quad , \qquad (2.2.25)$$

where r_s is the Wigner-Seitz radius:

$$r_s = \left(\frac{3}{4\pi n(\boldsymbol{r})}\right)^{1/3} \quad ; \qquad (2.2.26)$$

$$\zeta = \frac{n_\uparrow - n_\downarrow}{n} \quad , \qquad (2.2.27)$$

where ζ corresponds to the spin polarization; and

$$t = \frac{|\nabla n(\boldsymbol{r})|}{2\varphi(\zeta)k_s n(\boldsymbol{r})} \quad . \qquad (2.2.28)$$

Here,

$$\varphi(\zeta) = \frac{(1+\zeta)^{2/3} + (1-\zeta)^{2/3}}{2} \qquad (2.2.29)$$

is a spin-scaling factor, and

$$k_s = \sqrt{\frac{4k_F}{\pi}} \qquad (2.2.30)$$

is the Thomas-Fermi screening wave number, and

$$k_F = [3\pi^2 n(\boldsymbol{r})]^{1/3} \quad , \qquad (2.2.31)$$

is the radius of a sphere in k-space, such that the energy at the surface of the sphere is the Fermi energy. To satisfy the conditions of PBE, the Hamiltonian in Equation 2.2.25 is given by the ansatz:

$$H = \gamma\varphi^3 \ln\left[1 + \frac{\beta t^2}{\gamma}\left(\frac{1 + At^2}{1 + At^2 + A^2t^4}\right)\right] \quad , \qquad (2.2.32)$$

where $\gamma = 0.0.1091$, $\beta = 0.066725$, and the function

$$A = \frac{\beta}{\gamma e^{-\epsilon_C^{LDA}[n(\boldsymbol{r})]/\gamma\varphi^3} - 1} \quad . \tag{2.2.33}$$

For the exchange energy,

$$E_X^{GGA} = \int n(\boldsymbol{r})\,\epsilon_X^{LDA}[n(\boldsymbol{r})]\,F_X(s)\,d^3\boldsymbol{r} \quad , \tag{2.2.34}$$

where

$$F_X(s) = 1 + \kappa - \frac{\kappa}{1 + \mu s^2/\kappa} \quad . \tag{2.2.35}$$

Here, s is the dimensionless density gradient

$$s = \frac{|\nabla n(\boldsymbol{r})|}{2 k_F n(\boldsymbol{r})} \quad , \tag{2.2.36}$$

$\mu = 0.21951$, and $\kappa = 0.804$. Equations 2.2.25 and 2.2.34 summed together give the exchange and correlation energy for the PBE form of GGA.

While GGA makes approximations to compensate for any inadequacies of LDA, improvements and modifications are inevitable in the evolution of DFT. Since the trends of LDA and GGA are opposite in error to that of Hartree-Fock (HF) theory [21], hybrid approaches have evolved, where DFT is combined with HF, and the exchange-correlation energy is given by

$$E_{XC}^{hyb} = \alpha E_X^{HF} + (1 - \alpha) E_X^{DFT} + E_C^{DFT} \quad . \tag{2.2.37}$$

In this work the hybrid functional used is the HSE functional [33], which differs only slightly from Equation 2.2.37, and $\alpha = 0.25$.

2.3 The Projector Augmented Wave (PAW) Method and Pseudopotentials

With all of the energies taken into account in the Hamiltonian of the many-body problem, now it is time to focus on $\hat{V}_{ne}$ from Equation 2.1.9. Due to screening from the core electrons of atoms, the valence electrons experience a much weaker Coulomb potential than the electrons in the core shells. This classical property manifests in the wave function of an atom or ion: near the core, in the region of high Coulomb potential, the wave function oscillates with high frequency, while in the outer shell or bonding region the wave function is smoother with little oscillation. In order to model this phenomenon with the augmented-wave methods, the wave function is broken into parts: the atomic core, including the core electrons, is handled by a partial-wave expansion in a sphere surrounding the atomic nuclei, while the spherical shell surrounding or enveloping the core, including the valence electrons, is modeled with plane waves [34].

In the linear augmented-plane-wave method (LAPW), the wave function for the core is calculated by an ab initio self-consistent method based on atomic potentials from local-density-functional theory. The resulting wave function of the core is smoothed out into a pseudo wave function, ignoring the oscillation, in such a fashion that outside the core it is approximately identical to the real wave function. This is known as the frozen-core approach [34], [35].

In actuality, the valence wave functions in Hilbert space, which are orthogonal to the core, exhibit strong oscillations that make computational calculations difficult. These wave functions are the so-called all-electron (AE) wave functions, which are actually one-electron Kohn-Sham wave functions and not to be confused with a many-electron

wave function. Blöchl developed the PAW method in 1994 [34], which uses a linear transformation to map the AE wave functions to a pseudo (PS) Hilbert space, in order to make calculations more computationally convenient. A Hilbert space representation cannot be perfectly implemented numerically, so the AE wave functions are truncated in such a way to eliminate significant error. In order to maintain orthogonality, the PS wave functions must be truncated in exactly the same manner.

The linear transformation occurs inside an augmentation region, which is a region analogous to the frozen-core of the LAPW method. Outside of the augmentation region, the AE and PS wave functions coincide. Within an augmentation region, each PS one-electron wave function is composed of partial PS wave functions:

$$\|\tilde{\varphi}\rangle = \sum_i \|\tilde{\psi}_i\rangle c_i \quad . \tag{2.3.1}$$

Similarly, each AE one-electron wave function within the augmentation region is composed of partial AE wave functions:

$$\|\varphi\rangle = \mathrm{T}\|\tilde{\varphi}\rangle = \sum_i \|\psi_i\rangle c_i \quad , \tag{2.3.2}$$

where the T denotes the linear transformation from a PS to an AE wave function, and the c_i is the same coefficient in both 2.3.1 and 2.3.2, determined by

$$c_i = \langle \tilde{\boldsymbol{p}}_i \| \tilde{\varphi} \rangle \quad , \tag{2.3.3}$$

where $\tilde{p}_i$ are Blöchl's projector functions that minimize the total energy, with the condition

$$\langle \tilde{\boldsymbol{p}}_i \| \tilde{\psi}_j \rangle = \delta_{ij} \quad . \tag{2.3.4}$$

From 2.3.1, 2.3.2, and 2.3.3, the full representation of an AE one-electron wave function

in the PAW method becomes

$$\|\varphi\rangle = \|\tilde{\varphi}\rangle - \sum_i \|\tilde{\psi}_i\rangle c_i + \sum_i \|\psi_i\rangle c_i \quad . \tag{2.3.5}$$

Once transformed, the PS wave functions are the variational parameters instead of the AE wave functions.

2.4 Relativistic Effects: Scalar Orbital Radius Contraction and Spin-Orbit Interaction

The more familiar relativistic effects are those of increasing mass and length contraction due to a velocity approaching the speed of light. While electrons in s orbitals have zero orbital angular momentum, since

$$L^2\|l, m\rangle = l(l+1)\hbar^2\|l, m\rangle \quad , \tag{2.4.1}$$

and the quantum number $l = 0$ in the s orbital [36], the intrinsic angular momentum is non-zero. It is the zero orbital angular momentum which is the reason that s orbitals are nearer to the nucleus than their counterparts with the same quantum number n. Being closer to the nucleus gives them a much higher intrinsic angular momentum, and therefore gain the highest velocity [37]. In heavy elements such as mercury and lead, the velocity is so great, that relativistic effects need to be taken into account in the calculations. With this increase in velocity comes an increase in mass, resulting in orbital length contraction, increasing Coulomb attraction, which increases ionization energy. At high velocity and momentum, the relativistic kinetic energy becomes (for the moment, disusing Hartree units for illustrative purposes):

$$T = \sqrt{p^2 c^2 + m^2 c^4} - m c^2 \quad . \tag{2.4.2}$$

A McLauren series expansion of 2.4.2 leads to:

$$T = \frac{p^2}{2m} - \frac{p^4}{8 m^3 c^2} + \ldots \quad , \tag{2.4.3}$$

so the first order correction to the kinetic energy becomes

$$T_{rel} = -\frac{p^4}{8 m^3 c^2} \quad . \tag{2.4.4}$$

Equation 2.4.4 is treated as a perturbation in the calculation of PAWs.

Since valence s orbitals must be orthogonal to inner s orbitals, these orbital radii contract as well. This effect leads to what is known as an inert pair of s electrons [38], where the electrons in the outer s orbital are so deep in energy, that only the outer p orbital is available for bonding [37], [39]. For this reason, the bond in PbSe and PbTe is ionic.

The other scalar relativistic effect which affects the s orbitals, in a first order correction, is the so called Darwin term. In Dirac theory, an electron is smeared about the orbital due to small high frequency fluctuations – this is called zitterbewegung. The result is the extra term [40]

$$\hat{\boldsymbol{H}}_D = -\frac{e \hbar^2}{8 \mathrm{m}_e^2 c^2} \nabla^2 \quad , \tag{2.4.5}$$

which operates on s orbitals when calculating the PAW data.

A high magnitude of the intrinsic angular momentum has another atomic relativistic effect, as well – one which is more widely known – spin orbit interaction (SOI). Since the intrinsic angular momentum is due to spin, this high velocity has a

noticeable effect on eigenvalues of electrons in the same orbital – a splitting of degeneracy. In this case, the vector description of **L** is required to evaluate the effect, so the SOI is negligible in s orbitals; however, the effect can be seen clearly in p and d orbitals of heavier elements (Section 3.3). In the calculation of eigenvalues, the spin-orbit [20] operator,

$$\hat{\boldsymbol{H}}_{SO} = \frac{\hbar^2}{2\mathrm{m}_{rel}^2 c^2} \frac{1}{r} \frac{dV}{dr} \boldsymbol{L} \cdot \boldsymbol{\sigma} \quad , \tag{2.4.2}$$

is simply added to the other operators on the left-hand side of Equation 2.2.15, where **σ** represents the spinor. The mass m_{rel} denotes the increased relativistic mass of an electron with a high magnitude of intrinsic angular momentum at small r.

2.5 The Vienna Ab Initio Simulation Package (VASP)

From the atomic positions, their respective unit cells mentioned in the previous section, and the electronic configuration of the atom(s) in question, using Equations 2.2.6 and 2.3.5, theoretically, one can solve – by means of the iterative Kohn-Sham method (equations 2.2.6-16) – the many-body problem for the unit cell of a solid crystalline structure or for a single molecule. The unit cells in Section 1.2 may be considered an example, as calculations for any number of systems can be performed in exactly the same manner, assuming the atomic positions and PAWs are known.

Using the initial trial AE wave functions of each valence electron from Equation 2.3.5, a sub-space diagonalization using the Rayleigh-Ritz variational scheme (see Equation 2.2.1) is necessary:

$$\langle \varphi_j | \hat{\boldsymbol{H}} | \varphi_i \rangle = H_{ij} \quad . \tag{2.5.1}$$

A straightforward calculation for an exact diagonalization of the resulting Kohn-Sham Hamiltonian matrix would be extremely computationally demanding for large systems, but a clever approach was suggested by Car and Parrinello in 1985 [41]. They realized that both the total potential energy in real space and the kinetic energy in reciprocal space are diagonal already. Therefore, a calculation involving fast Fourier transformations (FFTs) back and forth from real space to reciprocal space optimizes computational time. An even more computationally efficient method is known as the self-consistent cycle (SC), where a mixing of the diagonalization of the Hamiltonian matrix using FFTs (Section 2.5.1) with an iterative scheme to determine charge density (Section 2.5.2) takes place. This method is used by VASP [24], [25].

2.5.1 Diagonalization of the Kohn-Sham Hamiltonian Matrix in VASP

In order to minimize computational time, each one-electron wave function is optimized at a time. The general idea is to find the error in the trial wave function in each iterative step, then that error is added to the trial wave function, resulting in a new trial wave function. This process, due to Rayleigh-Ritz, leads to more and more accurate eigenvalues, and the process is repeated until the desired accuracy is achieved. The eigenvalues are calculated [24], [25] as follows:

$$\epsilon_n = \frac{\langle \varphi_n | \hat{\boldsymbol{H}} | \varphi_n \rangle}{\langle \varphi_n | \hat{\boldsymbol{S}} | \varphi_n \rangle} \quad , \tag{2.5.2}$$

where the operator

$$\hat{\boldsymbol{S}} = 1 + \sum_{ij} q_{ij} \| \tilde{\boldsymbol{p}}_j \rangle \langle \tilde{\boldsymbol{p}}_i \| \quad , \tag{2.5.3}$$

using the localized projection states from the PAW method (Equations 2.3.3 and 2.3.4), with the familiar normalization condition:

$$\langle \varphi_n | \hat{\boldsymbol{S}} | \varphi_m \rangle = \delta_{nm} \quad . \tag{2.5.4}$$

The q_{ij} in Equation 2.5.3 is defined as

$$q_{ij} = \int Q_{ij}(\boldsymbol{r}) d^3 \boldsymbol{r} \quad , \tag{2.5.5}$$

where the Q_{ij} terms are localized augmentation functions. To find the error in the eigenvalue, the residual vector is introduced:

$$\| \boldsymbol{R}(\varphi_n) \rangle = (\hat{\boldsymbol{H}} - \epsilon_n \hat{\boldsymbol{S}}) \| \varphi_n \rangle \quad . \tag{2.5.6}$$

The error in the wave function is given by

$$\| \varphi_{error} \rangle = \left(\frac{1}{\hat{\boldsymbol{H}} - \epsilon_n} \right) \| \boldsymbol{R}(\varphi_n) \rangle \quad , \tag{2.5.7}$$

which cannot be solved exactly, since the kinetic energy dominates the Hamiltonian for large **G** vectors in k-space; i.e.,

$$\lim_{\boldsymbol{G} \to \infty} \hat{\boldsymbol{H}} = \frac{\boldsymbol{G}^2}{2} \quad . \tag{2.5.8}$$

Therefore, an approximation is used that tends to the above limit at large **G** and is constant for small **G**. The error is added to the trial wave function for the band in consideration, and the process begins with the next band. When all eigenvalues and wave functions are calculated for each band, the wave functions are orthogonalized by the Gram-Schmidt method, resulting in new trial wave functions for the following iteration. Finally, an update to the partial occupancies and charge density is performed, and the

whole process begins with the new wave functions and charge density, until the desired accuracy is reached.

2.5.2 Charge Density Mixing

The electronic density is modified by mixing the input and output charge densities in each iteration step. A residual vector of the electronic density is calculated [24], [25] by

$$\boldsymbol{R}[n_{in}(\boldsymbol{r})]=n_{out}[n_{in}(\boldsymbol{r})]-n_{in}(\boldsymbol{r}) \quad , \tag{2.5.9}$$

where n_{out} is a functional of n_{in}. The charge density calculation is modified from Equations 2.2.6 and 2.2.16 in the following manner:

$$n(\boldsymbol{r})=\sum_{n} f_n|\varphi_n(\boldsymbol{r})|^2+\sum_{n,ij} f_n\langle\varphi_n\|\tilde{\boldsymbol{p}}_j\rangle\langle\tilde{\boldsymbol{p}}_i\|\varphi_n\rangle Q_{ij}(\boldsymbol{r}) \quad , \tag{2.5.10}$$

where the n's run over all single electron orbitals, and f_n is the occupancy number one or zero. The essence of the mixing method is as follows:

$$n_{in}^{m+1}=n_{in}^{m}+A\,\boldsymbol{R}[n_{in}^{m}] \quad , \tag{2.5.11}$$

where m denotes the iteration step, and A can be determined from the eigenvalue (Section 2.5.1) spectrum. This calculation is very slow, so various schemes for mixing have arisen.

VASP uses the method of Pulay [24], [25], [42], in which all previous electronic densities in the loop are incorporated into the new optimized current density:

$$n_{in}^{opt}=\sum_{i}\alpha_i n_{in}^{i} \quad , \tag{2.5.12}$$

with the condition that

$$\sum_{i}\alpha_i=1 \quad . \tag{2.5.13}$$

The residual vector in the case of the Pulay method is

$$\boldsymbol{R}[n_{in}^{opt}] = \sum_i \alpha_i \boldsymbol{R}[n_{in}^{i}] \quad . \tag{2.5.14}$$

The new optimal charge density must minimize the norm of the residual vector:

$$\langle \boldsymbol{R}[n_{in}^{opt}] \| \boldsymbol{R}[n_{in}^{opt}] \rangle \quad . \tag{2.5.15}$$

The process is repeated iteratively, until the desired accuracy is reached.

CHAPTER 3:

STRUCTURAL, ELECTRONIC, AND MECHANICAL PROPERTIES OF PbSe AND PbTe

3.1 Parameters of Calculations

All ab initio calculations in this work were performed within DFT (Section 2.2), using the PAW method (Section 2.3) [34], via the VASP code (Section 2.5) [24], [25]. The PAW data includes the relativistic effects of lead (Section 2.4). The GGA exchange-correlation functionals of PBE [27], [28] were used. In all calculations, the 5d orbital of lead was included in the valence bands. A plane-wave basis set with an energy cut-off of 308.5 eV was used for complete k point convergence, minimizing total ground-state energy for all structures.

An automatically generated mesh of k points from the Monkhorst-Pack (MP) method was used in all self-consistent calculations [43]. It was found that in order to achieve minimum total energies, a different MP mesh needed to be used for the different phases of the two materials: for PbSe, a 16 x 16 x 16 mesh was used for the NaCl structure, a 6 x 10 x 10 mesh was used for the Pnma structure, and a 13 x 13 x 13 mesh was used for the CsCl structure; for PbTe, a 15 x 15 x 15 mesh was used for the NaCl structure, a 6 x 11 x 8 mesh was used for the Pnma structure, and a 9 x 9 x 9 mesh was used for the CsCl phase. In the case of the systems under pressure, cells were relaxed with the volumes held constant. In the supercell calculations of Section 3.5, a 3x3x3 MP

mesh was used. All of the systems studied were fully relaxed (ionic and electronic relaxations), with forces less than 10^{-5} eV/Å.

3.2 General Structural Properties of PbSe and PbTe from Total Energy Calculations

The lattice constants of the NaCl structures of PbSe and PbTe are well known to be 6.124 and 6.462 angstroms, respectively [44]. However, the lattice constants and ionic positions of the Pnma and CsCl structures are not as well established. Using data from the available literature [11], [12], [15], [45], here, unit cells of varying volume have been reproduced and relaxed, via ab initio calculations to minimize forces between ions, and total ground-state energies have been calculated. A Birch-Murnaghan [46], [47] curve fitting was employed to produce the equation of state:

$$E(V)=E_0+\frac{9V_0B_0}{16}\{[(\frac{V_0}{V})^{2/3}-1]^3B_0'+[(\frac{V_0}{V})^{2/3}-1]^2[6-4(\frac{V_0}{V})^{2/3}]\}\quad , \qquad (3.2.1)$$

where E is the total ground-state energy, V is the volume of the unit cell, E_0 is the minimum energy of the curve, V_0 is the volume corresponding to that minimum energy, B_0 is the bulk modulus

$$B=-V(\frac{\partial P}{\partial V})_T \quad , \qquad (3.2.2)$$

evaluated at P = 0, and

$$B_0'=[(\frac{\partial B}{\partial P})_T]_{B=B_0} \quad . \qquad (3.2.3)$$

The subscript T indicates constant temperature. The pressure in Equations 3.2.2 and 3.2.3

is given by

$$P = -\left(\frac{\partial E}{\partial V}\right)_S \quad , \tag{3.2.4}$$

where the subscript S denotes constant entropy. Therefore, the minimum of the curve, where the material is most stable and has the lowest energy, corresponds to zero pressure. The Birch-Murnaghan energy curves for the three phases of PbSe and PbTe can be seen in Figures 3.2.1a and 3.2.1b. As would be expected, since it takes energy to exert pressure on the materials, the higher-pressure phases have higher total ground-state energies.

Clearly, from equation 3.2.4, calculating total ground-state energy at different volumes will yield a different pressure from the derivative [20]. The Murnaghan fit of the fully relaxed structures reveals minimized lattice parameters which overestimate experimental data by 1.7% for the NaCl structures of both PbSe and PbTe at zero pressure. For the Pnma structures, the unit cells were relaxed with the volumes held constant, in order to obtain the correct aspect ratios of the lattice parameters. Lattice parameters were calculated at the pressures which they were observed experimentally (see Table 3.2.1); again, they overestimate by 1.7%. For the CsCl structures, the pressures at which the lattice parameters were measured are unclear, since the materials were grown on substrates [11], [12]. Here, the lattice parameters were calculated at the pressures at which the phase transitions have been found to occur experimentally (see Table 3.2.1). In the case of CsCl PbSe, the calculated lattice parameter overestimates experimental data by 1.7% again. It is typical for GGA calculations to overestimate optimized lattice parameters by 1-2% [20], [21]. In the case of CsCl PbTe, the calculated

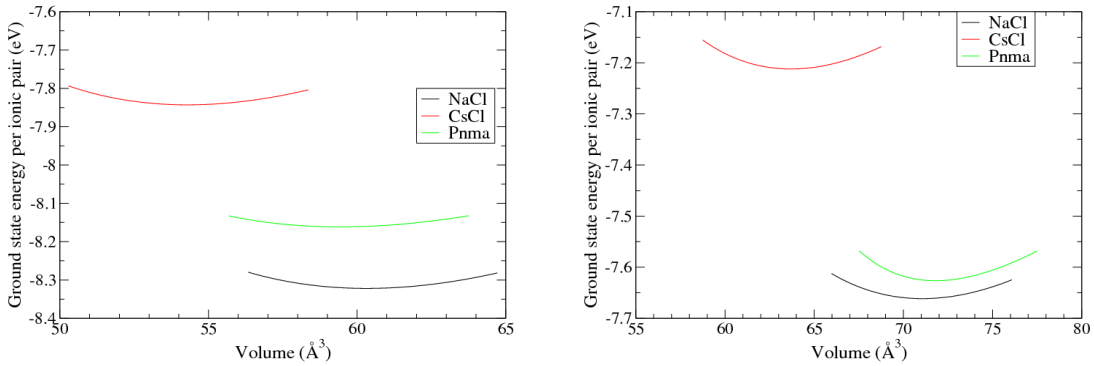

Figure 3.2.1. Total Energy vs Volume Curves for the 3 Phases of (a) PbSe and (b) PbTe. *For the purposes of comparison between the three phases, volumes and energies of the eight atom Pnma cells have been divided by four in order to normalize to two ions per cell.*

Table 3.2.1. Calculated Lattice Parameters for the Three Phases of PbSe and PbTe

		This Work				Experimental Data			
Material	Structure	Pressure (GPa)	a (Å)	b	c	Pressure (GPa)	a (Å)	b	c
PbSe	NaCl	0	6.226			0	6.124[a]		
	Pnma	9.5	11.37	4.24	4.12	9.5	11.19[b]	4.17[b]	4.06[b]
	CsCl	16	3.53			>16	3.49[c]		
PbTe	NaCl	0	6.573			0	6.462[a]		
	Pnma	6.7	8.31	4.57	6.33	6.7	8.18[d]	4.495[d]	6.23[d]
	CsCl	13	3.74			>13	3.55[e]		

a. O. Madelung, Semiconductors: Data Handbook, 3rd Edn., Springer, Berlin, Heidelberg (2004).
b. S. Streltsov, A. Manakov, A. Vokhmyanin, S. Ovsyannikov, and V. Shchennikov, J. Phys.: Condens. Matter 21 (2009) 385501.
c. M. Baleva and E Mateeva, J. Mater. Sci. Lett. 14 (1995) 158.
d. G. Rousse, S. Klotz, A. Saitta, J. Rodriguez-Carvajal, M. McMahan, B. Couzinet, and M. Mezouar, Phys. Rev. B 71 (2005) 224116.
e. M. Baleva and E Mateeva, , Phys. Rev. B 50 (1994) 8893.

Table 3.2.2 Calculated Atomic Positions of Pb, Se, and Te in Pnma Phases Under Pressure. *Positions are given as a percentage of unit cell length.*

			This Work		Experimental Data[a, b]	
Material	Structure	Pressure (GPa)	Position at 4c site (Pb)	Position at 4c site (Se, Te)	Position at 4c site (Pb)	Position at 4c site (Se, Te)
PbSe	Pnma	9.5	(0.1203, 0.25, 0.0006)	(0.1331, 0.75, 0.5005)	(0.1334,0.2500,0.0158)[a]	(0.1201,0.7500,0.5047)[a]
PbTe	Pnma	6.7	(0.5604, 0.25, -0.1977)	(0.8205, 0.75, 0.857)	(0.56,0.25,-0.19)[b]	(0.82,0.75,0.87)[b]

a. S. Streltsov, A. Manakov, A. Vokhmyanin, S. Ovsyannikov, and V. Shchennikov, J. Phys.: Condens. Matter 21 (2009) 385501.
b. G. Rousse, S. Klotz, A. Saitta, J. Rodriguez-Carvajal, M. McMahan, B. Couzinet, and M. Mezouar, Phys. Rev. B 71 (2005) 224116.

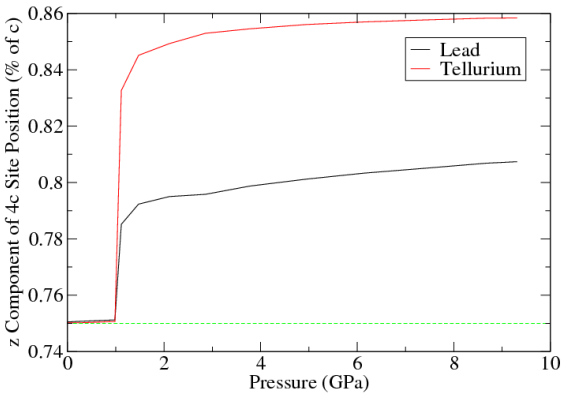

Figure 3.2.2. z Component of 4c Site Position vs Pressure of Pnma PbTe. *Here, it can be seen from the positions of the ions at the 4c site that the Pnma structure of PbTe relaxes to a distorted FCC structure at about 1 GPa. The instability and atomic shifting of the least symmetric phase of PbTe – as it seeks a more symmetric configuration – indicates the presence of soft phonon modes. Thus, a phonon contribution to the total ground-state energy is predicted.*

lattice parameter overestimates experimental results by 5.35%. This larger overestimation can be attributed to the unknown pressure exerted upon the material by the substrate when it was measured. See Table 3.2.1 for comparison of calculated lattice parameters with those of experiment.

The reader may observe from Figure 3.2.1b that the minimum energy of the Pnma phase of PbTe occurs at a slightly larger volume than that of the NaCl structure. In the NaCl and CsCl structures, the volume of the unit cell can be varied without changing atomic orientation relative to the cell; however, in the Pnma structure, the primitive cell's ions were found (in this work) to relax to more stable orientations when the volume was changed, indicating instability in the structure due to a presence of a soft phonon mode [48]. The displacement of the ions is much more pronounced in the PbTe structure than

the PbSe structure, and the displacement of the ions in Pnma PbTe at the 4c site is shown in Figure 3.2.2. The structure of Pnma PbTe relaxes to a distorted FCC cell at about 1 GPa. Therefore, the Pnma structure of PbSe is found to be metastable, whereas the Pnma structure of PbTe is unstable. In both cases, however, the transitions from NaCl (highly symmetric) to Pnma (less symmetric) to CsCl (highly symmetric) indicate the presence of soft phonon modes in the NaCl and Pnma structures. It has been shown recently that the NaCl structure has soft phonon modes, which have negative values for the Grüneisen parameter that contribute to the phase transition from NaCl to Pnma [49].

3.3 Structural Phase Transitions of PbSe and PbTe

In this section, the reliable method of plotting the pressure against the enthalpy [20], [50] is employed to find the structural phase transition pressures of PbSe and PbTe. The enthalpy is calculated as follows:

$$H = E + PV \quad , \tag{3.3.1}$$

where V was varied, and P was derived from Equation 3.2.4. The idea is to plot the enthalpy for all phases over a range of pressures; then, the structure with the lowest enthalpy at that pressure is the most stable. The pressure at which the enthalpy lines cross gives the structural phase transition pressure. Since the pressure range for the three phases is large, and the differences in enthalpy are rather small, it is easier to see transitions from a graph of pressure against the difference in enthalpy [see Figures 3.3a and 3.3b]. In this case, the pressure at which the transitions are calculated to occur corresponds to when the difference in enthalpy between two phases is zero.

As explained in the caption of Figure 3.2, the difference in the calculated transition pressures and the experimentally observed transition pressures can be attributed to the phonon contribution to the Helmholtz free energy. It is out of the scope of this work to calculate the phonon density of states, but the process of finding a more accurate transition pressure will be outlined here briefly. From calculations at each step of the ionic shifting in the Pnma phase, the phonon density of states can be calculated, using the method of Kunc and Martin [51]. Using a quasi-harmonic Debye model, the vibrational Helmholtz free energy A_{vib} can be calculated from the phonon density of states [52]. Then, enough information is available to calculate the non-equilibrium Gibbs energy:

$$G^* = E + PV + A_{vib} = H + A_{vib} \quad . \qquad (3.3.2)$$

The phase transition pressures could then be calculated using the same method as above, but with the more accurate non-equilibrium Gibbs energy, instead of the enthalpy. Since the NaCl and CsCl phases are stable, A_{vib} should be negligible, and G* would reduce to H. However, in the intermediate unstable Pnma phase, A_{vib} should be significant enough to shift G* to a lower energy than H, resulting in more accurate transition pressure calculations.

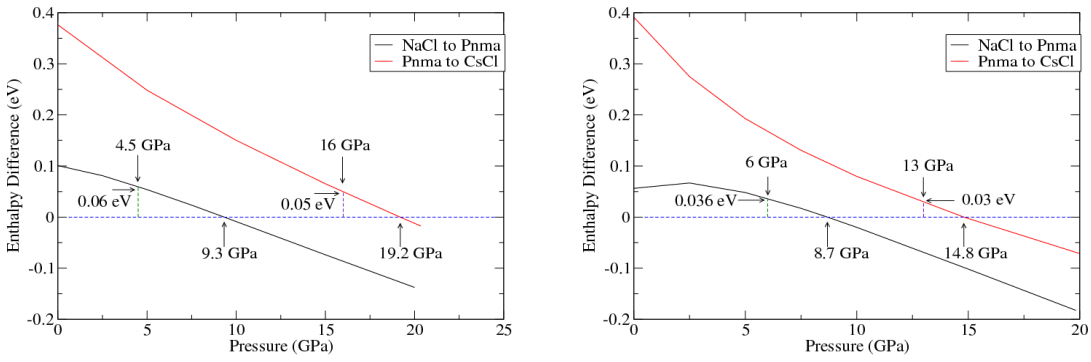

(a) **(b)**

Figure 3.3. Enthalpy Difference vs Pressure for the Three Phases of (a) PbSe and (b) PbTe. ***(a)*** *The black line shows the calculated enthalpy difference between the NaCl and Pnma phases. For PbSe, the line crosses 0 eV at a pressure of 9.3 GPa, corresponding to the structural phase transition from NaCl to Pnma. The arrow indicating 4.5 GPa is referring to the experimentally observed phase transition pressure. The difference in enthalpy of 0.06 eV can be attributed to the phonon contribution to the Helmholtz free energy. According to Equation 3.3.2, this has a direct effect on G*. Similarly, the red line shows the calculated enthalpy difference between the Pnma and CsCl phases at various pressures, where 19.2 GPa is the calculated phase transition pressure, and 16 is the phase transition pressure observed experimentally. Here, the enthalpy difference attributed to phonons is 0.05 eV. The graph for PbTe can be read in exactly the same way. The reader may notice a curve at the top of the black line. This is due to the shifting of ionic position in the Pnma phase of PbTe at various volumes (pressures) during relaxation, thus affecting the total ground-state energy calculations.*

3.4 Band Structures, Splittings, Band Gaps, and Density of States for PbSe and PbTe Under Pressure

The band structures of PbSe and PbTe in the NaCl structure (Figures 3.4.1a and 3.4.1b) are well-known. Using the 2-atom primitive cell of Equation 1.2.3 and Figure 1.2.1c, the Brillouin zone and common path traced is that of Figure 1.2.4a. As is clear from Figure 3.4.1, the band gap is at the L point in both materials, which are narrow-gap semiconductors. From the adjacent graph with total density of states (TDOS) and partial

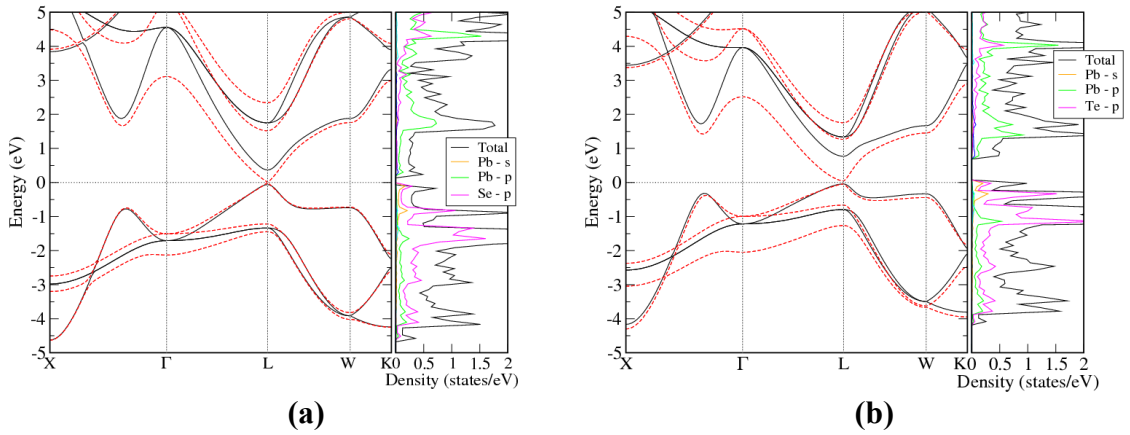

Figure 3.4.1. Band Structure and Density of States of the NaCl Structures of (a) PbSe and (b) PbTe. *Both structures are narrow-gap semiconductors and are calculated at zero pressure, i.e., with lattice parameters which minimize the total energy. The black lines in the band structure are without SOI, whereas the red dotted lines are with SOI. In both cases the band gap is at the L point, and the conduction bands are dominated by the p orbital of Pb, while the valence bands are dominated by p orbitals of Se (a) and Te (b). The s orbitals of Se and Te are not significant in the region shown.*

densities of states (PDOS), it can be seen that the valence bands are mostly composed of the p orbitals of selenium (3.4.1a) and tellurium (3.4.1b). The conduction bands in both cases are mostly from the p orbitals of lead.

If one looks closely, the second lowest conduction band (2nd LCB) and the second highest valence band (2nd HVB) exhibit splitting at the L point when SOI (Section 2.4) is taken into account in the calculation. In these bands, splitting occurs throughout the paths traced in the Brillouin zones. The resultant gaps are summarized in Table 3.4 and compared to experimental results [53], [54] for the Γ and X points. The splitting comparisons indicate the accuracy of the method used.

Table 3.4 Splittings of 2nd HVB and 2nd LCB in PbSe and PbTe Due to SOI. *Splitting is measured in eV.*

	This Work				Experiment[a]		Experiment[b]	
NaCl	@L point Eg 2nd LCB	@L point Eg 2nd HVB	@Gamma Eg 2nd HVB	@X Eg 2nd HVB	@Gamma Eg 2nd HVB	@X Eg 2nd HVB	@Gamma Eg 2nd HVB	@X Eg 2nd HVB
PbSe	0.8252	0.2297	0.6259	0.4551	0.6	0.5	0.75	0.55
PbTe	0.4883	0.5978	1.0531	0.6666	1.15	0.9	1.1	1.1

a. T. Grandke, L. Ley, M. Cardona, Phys. Rev. B 18 (1978) 3847.
b. V. Hinkel, H. Haak, C. Mariani, L. Sorba, and K. Horn, Phys. Rev. B 40 (1989) 5549.

The key detail to notice in the band structures of the Pnma phases (Figure 3.4.2) is that the band gap becomes indirect. However, from the density of states, it can be seen that the character of the bands, i.e., the dominant orbitals contributing to each band, remains mostly the same. In PbSe, the lowest point in the LCB can be found between the Y and Γ points in the Brillouin zone. The highest point in the HVB can be found between the Γ and Z points. In PbTe, the lowest point in the LCB is between the Γ and Z points, and the highest point in the HVB is precisely at the T point. Calculating the band gaps at varying pressures – using GGA with SOI – in this phase is fairly straightforward, and the trend clearly indicates that the band gap decreases with increasing pressure in this phase (Figure 3.4.3), as is found experimentally [16].

For the NaCl phase, it has been reported recently [55] that the band gap inverts when using an LDA calculation with SOI. While the calculations of the band structures in Figure 3.4.1 were performed using GGA, it is not always an improvement over LDA, as can be seen from the closure of the band gap when including SOI. Furthermore, no decipherable trend could be found when varying the pressure with SOI. Therefore, for this phase, the HSE functional was employed with SOI, and the trend of decreasing band gap with increasing pressure – that has been observed experimentally – is confirmed here

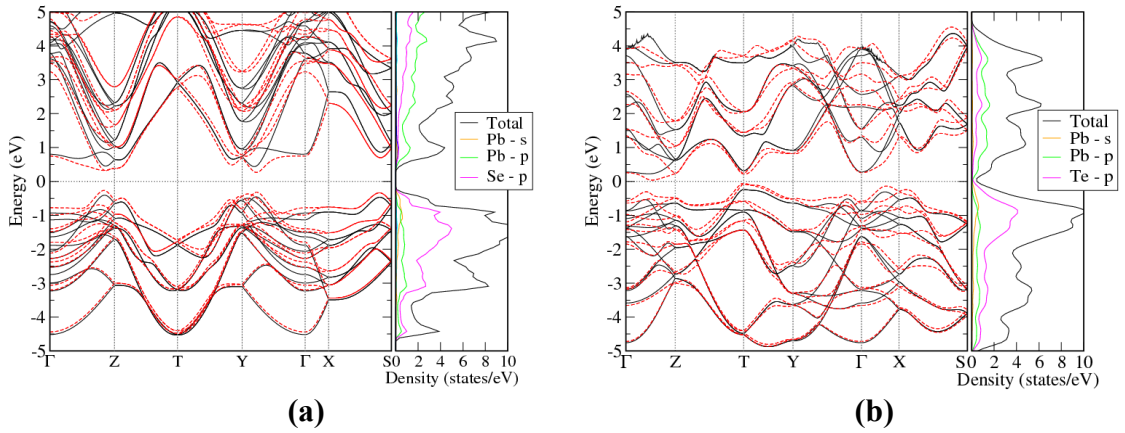

Figure 3.4.2. Band Structure and Density of States for the Pnma Structures of (a) PbSe and (b) PbTe Under Pressure. *The band structures of Pnma PbSe at 9.5 GPa and PbTe at 6.7 GPa clearly show indirect band gap semiconductors. While the overall structure is different in the two cases, the character of the bands is very similar.*

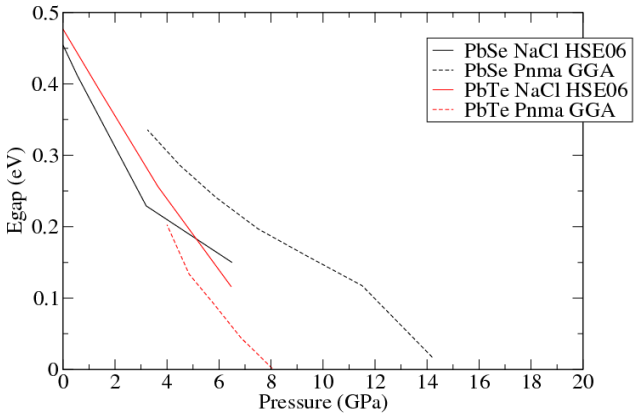

Figure 3.4.3. Energy Band Gap vs Pressure for NaCl and Pnma PbSe and PbTe. *The overlap between the phases is due to the uncertainty of the exact transition pressure.*

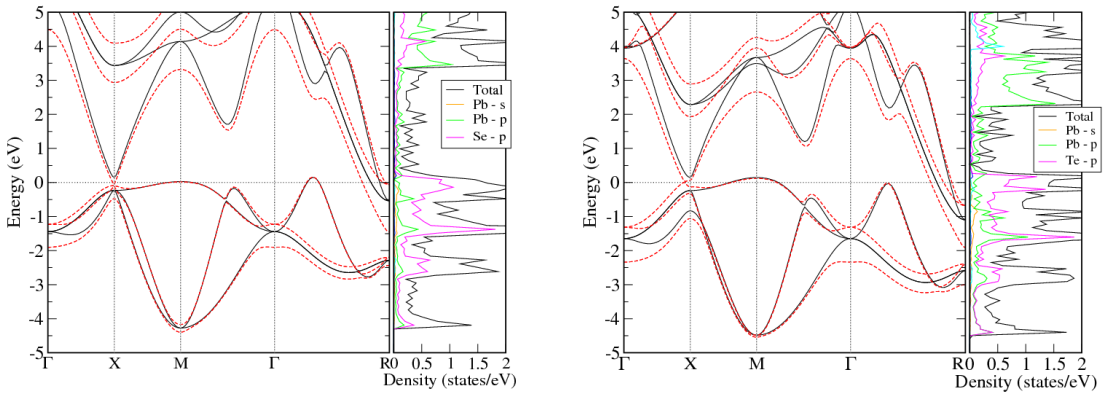

Figure 3.4.4. Band Structure and Density of States for the CsCl Structures of (a) PbSe and (b) PbTe Under Pressure. *PbSe at 16 GPa and PbTe at 13 GPa are clearly conductors, since the conduction band crosses the Fermi level in both cases. The character of the bands remains similar in all phases in both materials.*

theoretically (Figure 3.4.3). While the calculations here overestimate the band gap in the NaCl phase with HSE and underestimate the gap in the Pnma case with GGA, the trend is clearly linear and in agreement with experiment. Furthermore, the band gap is larger in PbTe than PbSe in the NaCl phase, and the gap is larger in PbSe than PbTe in the Pnma phase, as in experiment. The measured band gaps of PbSe and PbTe in the NaCl phase at 4 K are 0.145 eV and 0.1715 eV, respectively [44]. The band gaps of PbSe and PbTe in the Pnma phase are unknown at low temperature, but at 273 K they are known for various pressures: PbSe peaks at about 0.4 eV at 6 GPa, and PbTe peaks at about 0.1 eV at 7 GPa. The CsCl structure was not included in Figure 3.4.3, because as can be seen from Figure 3.4.4, it is a conductor. However, the thermoelectric applicability of the CsCl phase is unknown.

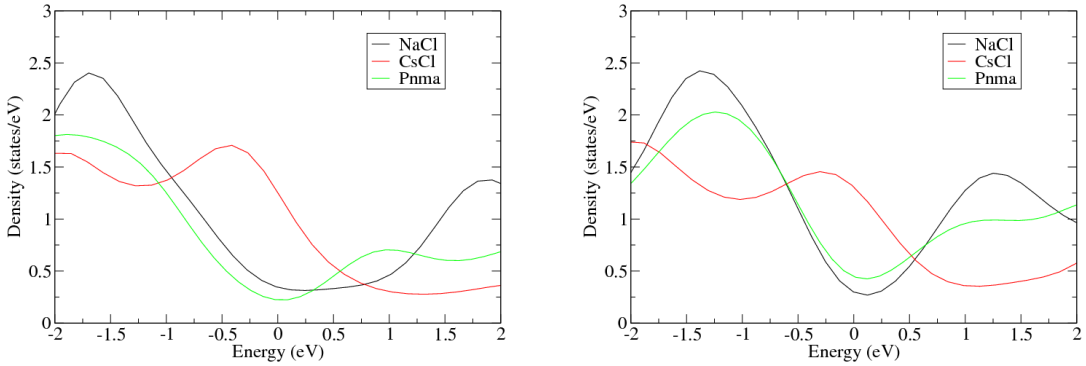

Figure 3.4.5. Total Density of States for the Three Phases of (a) PbSe and (b) PbTe. *The Density of states of the Pnma phase has been normalized to 2 atoms in both cases. The Pnma and CsCl phases are under pressure. Smearing values are greater here than in Figures 3.1.1, 3.1.2, and 3.1.4.*

Improvement of thermoelectric efficiency can be predicted by analyzing the rate of increase of TDOS near the band gap [56]. For PbTe, the results shown in Figure 3.4.5b agree with previous calculations that the Pnma phase has a slightly greater rate of increase in TDOS near the VBM than the NaCl phase [57]. However, both the phases have a sharp increase at the VBM, so p-type doping could enhance thermoelectric efficiency in either case. The increase at the CBM is promising for n-type doping, as well, but the increase is not as great. For PbSe, the results shown in Figure 3.4.5a predict an enhancement of thermoelectric efficiency with p-type doping in the NaCl phase, while the Pnma phase of PbSe looks like a promising candidate for both n-type and p-type doping.

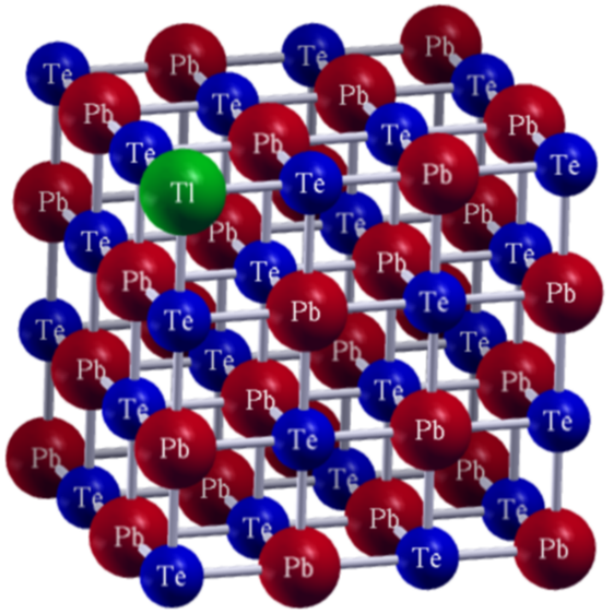

Figure 3.5. Supercell with Impurity. *Example of a 64 atom supercell used in calculations in Section 3.5. Here, one Pb atom is replaced by one Tl atom, resulting in a p-type material. The PbSe supercells have the same atomic orientation, with each Te atom being replaced by Se. Other impurities replace Pb, as well, with the exception of I, which replaces a Se or Te atom in PbSe or PbTe, respectively.*

3.5 Mechanical Properties of n- and p-type PbSe and PbTe in the NaCl

Structure

Part of the problem with using PbSe and PbTe in thermoelectric devices is their brittle nature. Hardness has been measured for NaCl PbTe and its related alloys, with and without dopants, in several cases, and it was found that brittleness is often associated with a higher Vicker's hardness value, and a more ductile material – which is a desirable attribute in a thermoelectric material – typically has a lower hardness [55–62]. Doping

the alloy $Pb_{1-x}Sn_xTe$, with the p-type impurity Na, is found to decrease the zT value [62–65]; furthermore, Gelbstein, et al. [61] have found that doping intrinsic PbTe with p-type Na increases the hardness and brittleness, while doping with In or PbI_2 has no noticeable effect.

Since PbSe is found to be brittle [66], but available data in the literature is sparse, mechanical properties are calculated here for intrinsic and doped NaCl PbSe and PbTe. In order to simulate experimental dopant concentrations of about 10^{20} cm^{-3}, which is an order of magnitude higher than is optimal for practical applications [62], the ab initio calculations of this work use 64 atom cubic supercells (Figure 3.5). To achieve lower impurity concentrations, larger supercells would need to be used, but the trends can be evaluated effectively with concentrations similar to 10^{20} cm^{-3}. One Pb atom is replaced by an impurity, with the exception of I, which replaces one Se or Te. Using Na, In, and Tl (p-type) and Bi and I (n-type) as dopants, which all contribute either one electron or one hole, corresponds to a carrier concentration of approximately 5 x 10^{20} cm^{-3}. Second-order elastic moduli were derived from total ground-state energy calculations (Appendix A). From these values, bulk moduli (B), shear moduli (G), Young's moduli (E), and Poisson ratios (υ) were calculated using the Reuss-Voigt-Hill method [67] (Appendix B). The Pugh ratio, which can be found from G/B, indicates brittleness when $G/B > 0.57$ and ductility for $G/B < 0.57$ [68]. All of the above quantities are summarized in Table 3.5.1 and compared, when possible, to experimental values [44], [60].

Table 3.5.1. Mechanical Properties of NaCl PbSe and PbTe (Doped and Intrinsic). *Experimental values are for single crystals. For doped systems, x = 0.03125. The lattice parameter a is in Å, and elastic constants and moduli are in GPa.*

NaCl

	Type	a	C11	C12	C44	B	G	E	Poisson	G/B	Behavior
Experiment											
PbTe	intrinsic	6.462[a]	105.32[a]	7.02[a]	13.221[a]	38.39[a]	22.95[b]	58.05[b]	0.264[b]	0.598	brittle
This Work											
PbTe 2 atom cell	intrinsic	6.567	103.94	5.4922	14.0466	38.308	23.89	59.34	0.2418	0.624	brittle
PbTe 64 atom cell	intrinsic	6.567	103.234	5.42955	13.8588	38.031	23.65	58.77	0.2424	0.622	brittle
$Pb_{1-x}Na_xTe$	p	6.269	217.786	22.4058	26.3142	87.53	46.02	117.48	0.2763	0.526	ductile
$Pb_{1-x}Tl_xTe$	p	6.548	102.677	6.29238	12.6398	38.42	22.4	56.26	0.256	0.583	brittle
$Pb_{1-x}Bi_xTe$	n	6.55	104.259	5.69577	10.779	38.55	20.93	53.17	0.2701	0.543	ductile
$Pb_{1-x}In_xTe$	p	6.544	104.478	5.21232	13.3669	38.3	23.38	58.28	0.2464	0.61	brittle
$PbTe_{1-x}I_x$	n	6.563	100.383	6.33108	8.92641	37.68	18.69	48.11	0.2872	0.496	ductile
Experiment											
PbSe	intrinsic	6.124[a]	123.75[a]	19.34[a]	15.92[a]						
This Work											
PbSe 2 atom cell	intrinsic	6.2256	114.833	12.3765	17.1202	46.529	27.05	67.98	0.2565	0.581	brittle
PbSe 64 atom cell	intrinsic	6.2256	114.53	11.4307	16.904	45.797	26.94	67.57	0.2541	0.588	brittle
$Pb_{1-x}Na_xSe$	p	5.938	243.18	32.3728	30.5925	102.64	51.62	132.62	0.2846	0.503	ductile
$Pb_{1-x}Tl_xSe$	p	6.202	111.839	10.7301	15.5005	44.43	25.49	64.19	0.2592	0.574	brittle
$Pb_{1-x}Bi_xSe$	n	6.202	115.448	9.42395	13.8328	44.77	24.57	62.31	0.268	0.549	ductile
$Pb_{1-x}In_xSe$	p	6.197	111.654	6.83942	16.3875	41.78	26.7	66.03	0.2366	0.639	brittle
$PbSe_{1-x}I_x$	n	6.225	112.339	9.24434	12.6379	43.61	23.15	59.01	0.2745	0.531	ductile

a. O. Madelung, Semiconductors: Data Handbook, 3rd Edn., Springer, Berlin, Heidelberg (2004).

b. J. E. Ni, et al. Materials Science and Engineering B 170 (2010) 58–66 .

Before calculating elastic constants for the doped systems, they were calculated in the intrinsic 2 atom cells with a dense k point mesh – 16x16x16 for PbSe and 15x15x15 for PbTe. Finding these values within reasonable range of the experimental values from the literature, they were compared to calculations of the intrinsic material using a 64 atom unit cell and a 3x3x3 k point mesh. Since all elastic constants in the supercells came within 1.3% of values in the 2 atom cells, with the exception of C_{12} of PbSe, which was off by 7.6%, the calculations of the doped systems are more than sufficient for analyzing trends. To achieve identical results would require a higher number of k points in the supercell, which was not possible in these calculations, due to limitations in

Table 3.5.2. Elastic Constants and Moduli for the Pnma Structures of PbSe and PbTe. *Quantities are measured in GPa.*

Pnma									
	C11	C12	C13	C22	C23	C33	C44	C55	C66
PbSe	91.9603	22.2255	12.3191	92.272	65.1182	96.3791	18.8646	70.9043	4.40652
PbTe	67.4009	43.2831	19.9225	73.4444	32.5082	81.4094	65.8156	23.6703	19.8131

	B	G	E	Poisson	G/B
PbSe	52.2	21.9	57.65	0.3159	0.42
PbTe	45.55	26.51	66.6	0.2563	0.582

Table 3.5.3. Elastic Constants and Moduli for the CsCl Structures of PbSe and PbTe. *Quantities are measured in GPa.*

CsCl								
	C11	C12	C44	B	G	E	Poisson	G/B
PbSe	167.792	57.8421	26.5704	94.49	35.71	95.19	0.3322	0.378
PbTe	90.4056	69.3775	29.2705	76.39	19.42	53.72	0.3828	0.254

computational resources. It should be noted that in the Na doped case, the lattice parameters decrease by about 5%. It is unclear whether or not this is observed experimentally; however, when relaxations are performed without changing lattice constants, PbSe and PbTe with the Na impurity are found to be brittle.

That being said, with the exception of the fully relaxed Na doped system, the results calculated here are in excellent agreement with the available experimental data in the literature. Looking at the G/B Pugh ratios, it can be concluded that the Na, I, and Bi doped materials become significantly more ductile, and In and Tl doped materials retain the brittleness of their intrinsic counterparts. Na and In doped PbTe hardness values are known experimentally [59], [61] but are not as well-known for Bi and Tl doped PbTe. Furthermore, PbSe has not been studied nearly as extensively as PbTe. Low brittleness would be particularly important for Tl doped PbSe and PbTe, since they have excellent potential thermoelectric applicability. However, the calculations performed in this work indicate that both Tl doped PbSe and PbTe are right on the borderline between ductility

and brittleness, with PbTe being slightly more brittle and both slightly more ductile than their intrinsic materials.

The calculations summarized in Table 3.5.1 were carried out for intrinsic Pnma and CsCl PbSe and PbTe, as well. The results are listed in Tables 3.5.2-3. The results indicate that all cases are ductile, except for Pnma PbTe. Due to the TDOS of Pnma PbSe indicating enhancement of zT by doping, and the finding that Pnma PbSe is more stable than its PbTe counterpart, the high ductility of this phase is very promising for applications.

CHAPTER 4:

CONCLUDING REMARKS

A summary of DFT was given – using PAWs and employing GGA for exchange and correlation – followed by an explanation of how DFT is implemented in the VASP code. VASP was used for all calculations of total ground-state energy and eigenvalues in this work. Effects of pressure on structural parameters, structural phase transitions, and electronic and mechanical properties of PbSe and PbTe were studied and found to agree very well with available experimental data, and the predictions found here should foster further developments in the field. Pressures were obtained by varying the lattice parameters in the three phases of PbSe and PbTe and taking the derivative of the energy in the Birch-Murnaghan equation of state.

The calculated lattice parameters agree remarkably well with reported values in the literature, for all phases of both materials. The Pnma phase of PbSe was found to be metastable, with a TDOS indicating possible thermoelectric enhancement from n-type doping, while Pnma PbTe was found to be unstable. Furthermore, the calculated Pugh ratio revealed that Pnma PbSe is very ductile, so it is concluded here that further thermoelectric studies of PbSe Pnma are warranted. Due to the increased thermoelectric possibilities of both materials under pressure, it is important to determine a precise transition pressure from NaCl to Pnma. Here, it was found that phonons play an

important role in the NaCl and Pnma phases of PbSe and PbTe, and approximations to the phonon contribution to the non-equilibrium Gibbs energy in the Pnma phase were made. Further studies are under way to determine a more precise phonon contribution to the non-equilibrium Gibbs energy of the intermediate phases, and thus find more accurate transition pressures in group IV-VI semiconductors.

Pressure effects on the band structures and band gaps have been calculated for PbSe and PbTe, and experimental findings that the band gap decreases with pressure have been confirmed. Splitting, of the 2^{nd} HVB and the 2^{nd} LCB bands at various symmetry points in the Brillouin zone of zero pressure NaCl PbSe and PbTe, due to SOI, has been observed. The differences in eigenvalues at those points have been calculated and compared with available experimental results, all confirming the accuracy of the methods used.

Calculations of brittleness in doped NaCl PbTe confirm experimental results, while those of PbSe are ready to be confirmed by experiment. Thallium doped PbSe and PbTe, which have a high zT value, were found to be slightly more ductile than their intrinsic counterparts but still brittle. The calculations in this work suggest that Iodine doped PbSe and PbTe may withstand pressure without substantial structural damage; therefore, their thermoelectric efficiency should be evaluated under pressure in future studies.

APPENDIX A:

CALCULATION OF SECOND ORDER ELASTIC MODULI

The elastic constant tensor is a 6x6 matrix, where each term in the matrix has units of pressure and is the second derivative of the total ground-state energy between atoms [69], with respect to stress tensor components λ, divided by the volume V:

$$C_{ij} = \frac{1}{V}\left(\frac{\partial^2 E}{\partial \lambda_i \partial \lambda_j}\right) \quad . \qquad \text{(A.1)}$$

The subscripts of λ indicate the six possible variations in atomic position coordinates. For example, in a simple cubic system, if i = xx and j = xx, this would correspond to the strain on the cube when force is applied in the x direction to the face of the cube that is normal to the x axis. C_{yx} is the strain on the cube when force is applied in the y direction to the face of the cube that is normal to the x axis. C_{zx} is analogous to C_{yx}, etc. This force can be applied via ab initio methods by changing the atomic positions to non-equilibrium locations. The other three values for i and j (i.e., i = xy and/or j =zx) correspond to orthorhombic and monoclinic distortions to the cube.

APPENDIX B:

CALCULATION OF B, G, E, AND υ

Following the Reuss-Voigt-Hill approximation [67], B, G, E, and υ are calculated from the elastic constants of Appendix A by two different methods and then averaged together. Here, Voigt notation will be used, where 1 = xx, 2 = yy, 3 = zz, 4 = xy, 5 = yz, and 6 = zx. The following equations were taken directly from Aydin, et al. [70], and have been shown to be effective in Pnma symmetries [71]:

$$B_V = \frac{1}{9}[C_{11} + C_{22} + C_{33} + 2(C_{12} + C_{13} + C_{23})] \quad ; \tag{B.1}$$

$$G_V = \frac{1}{15}[(C_{11} + C_{22} + C_{33}) + 3(C_{44} + C_{55} + C_{66}) - (C_{12} + C_{13} + C_{23})] \quad ; \tag{B.2}$$

$$B_R = \Delta\big[C_{11}(C_{22} + C_{33} - 2C_{23}) + C_{22}(C_{33} - 2C_{13}) - 2C_{33}C_{12} + C_{12}(2C_{23} - C_{12})C_{13}(2C_{12} - C_{13}) + C_{23}(2C_{13} - C_{23})\big]^{-1} \quad ; \tag{B.3}$$

$$G_R = 15\Big\{4\big[C_{11}(C_{22} + C_{33} + C_{23}) + C_{22}(C_{33} + C_{13}) + C_{33}C_{12} - C_{12}(C_{23} + C_{12}) - C_{13}(C_{12} + C_{13}) - C_{23}(C_{13} + C_{23})\big]\Big\}/\Delta + 3/\left(\frac{1}{C_{44}} + \frac{1}{C_{55}} + \frac{1}{C_{66}}\right) \quad ,\tag{B.4}$$

where

$$\Delta = C_{13}(C_{12}C_{23} - C_{13}C_{22}) + C_{23}(C_{12}C_{13} - C_{23}C_{11}) + C_{33}(C_{11}C_{22} - C_{12}^2) \quad . \tag{B.5}$$

Finally,

$$B = \frac{B_V + B_R}{2} \quad ; \tag{B.7}$$

$$G = \frac{G_V + G_R}{2} \quad ; \tag{B.8}$$

$$E = \frac{9\,B\,G}{3\mathrm{B} + G} \quad ; \tag{B.9}$$

and,

$$\nu = \frac{3\mathrm{B} - 2\mathrm{G}}{2(3\mathrm{B} + G)} \quad . \tag{B.10}$$

REFERENCES

[1] E. A. S. and D. S. Trimmer, *CRC Handbook of Thermoelectrics*. Boca Raton: CRC Press, 1995, pp. 267–275.

[2] G. J. Snyder and E. S. Toberer, "Complex thermoelectric materials.," *Nature Materials*, vol. 7, no. 2, pp. 105–14, Feb. 2008.

[3] J. Heremans, V. Jovovic, and E. Toberer, "Enhancement of thermoelectric efficiency in PbTe by distortion of the electronic density of states," *Science*, vol. 321, p. 554, 2008.

[4] D. Parker and D. Singh, "High-temperature thermoelectric performance of heavily doped PbSe," *Physical Review B*, vol. 82, no. 3, p. 035204, Jul. 2010.

[5] S. V. Ovsyannikov and V. V. Shchennikov, "Pressure-tuned colossal improvement of thermoelectric efficiency of PbTe," *Applied Physics Letters*, vol. 90, no. 12, p. 122103, 2007.

[6] S. V. Ovsyannikov and V. V. Shchennikov, "High-Pressure Routes in the Thermoelectricity or How One Can Improve a Performance of Thermoelectrics †," *Chemistry of Materials*, vol. 22, no. 3, pp. 635–647, Feb. 2010.

[7] Y. Wang, X. Chen, T. Cui, Y. Niu, Y. Wang, M. Wang, Y. Ma, and G. Zou, "Enhanced thermoelectric performance of PbTe within the orthorhombic Pnma phase," *Physical Review B*, vol. 76, no. 15, pp. 1–10, Oct. 2007.

[8] V. V. Shchennikov, S. V. Ovsyannikov, and a. Y. Derevskov, "Thermopower of lead chalcogenides at high pressures," *Physics of the Solid State*, vol. 44, no. 10, pp. 1845–1849, Oct. 2002.

[9] L. Vereshchagin and S. Kabalkina, *X-ray Diffraction Studies under High Pressure*. Moscow: Nauka, 1977.

[10] A. Grzechnik and K. Friese, "Pressure-induced orthorhombic structure of PbS.," *Journal of physics. Condensed Matter : an Institute of Physics journal*, vol. 22, no. 9, p. 095402, Mar. 2010.

[11] M. Baleva and E. Mateeva, "Detection of the metastable TII-type phase of PbSe in films grown by electron beam evaporation: I. X-ray diffraction," *Journal of Materials Science Letters*, vol. 14, pp. 158–160, 1995.

[12] M. Baleva and E. Mateeva, “Pressure coefficient of the PbTe metastable CsCl-type-phase energy gap,” *Physical Review B*, vol. 50, no. 12, pp. 8893–8896, 1994.

[13] Ashcroft and Mermin, *Solid State Physics*. Brooks/Cole, 1976.

[14] A. Kokalj, “XCrySDen--a new program for displaying crystalline structures and electron densities.,” *Journal of Molecular Graphics & Modelling*, vol. 17, no. 3–4, pp. 176–9, 215–6, 2000.

[15] G. Rousse, S. Klotz, a. Saitta, J. Rodriguez-Carvajal, M. McMahon, B. Couzinet, and M. Mezouar, “Structure of the intermediate phase of PbTe at high pressure,” *Physical Review B*, vol. 71, no. 22, pp. 1–6, Jun. 2005.

[16] S. V. Ovsyannikov, V. V. Shchennikov, A. Y. Manakov, A. Y. Likhacheva, Y. S. Ponosov, V. E. Mogilenskikh, A. P. Vokhmyanin, A. I. Ancharov, and E. P. Skipetrov, “Unusual B1-B2 transition in PbSe under high pressure: evidence for two intermediate phases; transport, structural, and optical properties,” *Physica Status Solidi (B)*, vol. 246, no. 3, pp. 615–621, Mar. 2009.

[17] W. Harrison, *Solid State Theory*. New York: , 1980.

[18] H. Goldstein, C. Poole, and J. Safko, *Classical Mechanics*, 3rd ed. San Francisco: Addison Wesley, 2002.

[19] J. D. Jackson, *Classical Electrodynamics, 3rd ed.*, 3rd ed. Hoboken: John Wiley and Sons Inc., 1999.

[20] R. M. Martin, *Electronic Structure*. New York: Cambridge University Press, 2004.

[21] J. Kohanoff, *Electronic Structure Calculations for Solids and Molecules*. Cambridge: Cambridge University Press, 2006.

[22] P. Hohenberg and W. Kohn, “Inhomogeneous electron gas,” *Physical Review*, vol. 136, p. B864, 1964.

[23] W. Kohn and L. Sham, “Self-Consistent Equations Including Exchange and Correlation Effects,” *Physical Review*, vol. 140, no. 4A, p. A1133, 1965.

[24] G. Kresse and J. Furthmüller, “Efficiency of ab-initio total energy calculations for metals and semiconductors using a plane-wave basis set,” *Comput. Mat. Sci.*, vol. 6, pp. 15–50, 1996.

[25] G. Kresse and J. Furthmüller, “Efficient iterative schemes for ab initio total-energy calculations using a plane-wave basis set.,” *Physical Review B,* vol. 54, no. 16, pp. 11169–11186, Oct. 1996.

[26] B. Alder and D. Ceperly, “Ground State of the Electron Gas by a Stochastic Method,” *Physical Review Letters*, vol. 45, no. 7, p. 56, 1980.

[27] J. Perdew, K. Burke, and M. Ernzerhof, “Generalized Gradient Approximation Made Simple.,” *Physical Review Letters*, vol. 77, no. 18, pp. 3865–3868, Oct. 1996.

[28] J. Perdew, K. Burke, and M. Ernzerhof, “Generalized Gradient Approximation Made Simple.,” *Physical Review Letters*, vol. 78, no. 7, p. 1396, Oct. 1997.

[29] C. Filippi, D. Singh, and C. Umrigar, “All-electron local-density and generalized-gradient calculations of the structural properties of semiconductors,” *Physical Review B*, vol. 50, no. 20, pp. 947–951, 1994.

[30] K. Brueckner, S. Ma, “Correlation energy of an electron gas with a slowly varying high density,” *Physical Review*, vol. 165, no. 1, p. 18, 1968.

[31] D. Langreth and M. Mehl, “Easily implementable nonlocal exchange-correlation energy functional,” *Physical Review Letters*, vol. 47, no. 1974, pp. 446–450, 1981.

[32] J. P. Perdew, “Accurate Density Functional for the Energy: Real-Space Cutoff of the Gradient Expansion for the Exchange Hole,” *Physical Review Letters*, vol. 55, no. 16, pp. 1665–1668, 1985.

[33] J. Heyd and G. E. Scuseria, “Efficient hybrid density functional calculations in solids: assessment of the Heyd-Scuseria-Ernzerhof screened Coulomb hybrid functional.,” *The Journal of Chemical Physics*, vol. 121, no. 3, pp. 1187–92, Jul. 2004.

[34] P. Blöchl, “Projector augmented-wave method,” *Physical Review B*, vol. 50, no. 24, p. 17953, 1994.

[35] D. Hamann, “Generalized norm-conserving pseudopotentials,” *Physical Review B*, vol. 40, no. 5, p. 2980, 1989.

[36] J. Sakurai and J. Napolitano, *Modern quantum mechanics*, 2nd ed. Boston: , 1994.

[37] P. Christiansen, W. Ermler, and K. Pitzer, “Relativistic Effects in Chemical Systems,” *Annual Review of Physical Chemistry*, vol. 36, no. 1, pp. 407–432, Jan. 1985.

[38] N. Sidgwick, *The electronic theory of valency*. Clarendon: Oxford, 1927.

[39] S. Biering and P. Schwerdtfeger, “A comparative density functional study of the high-pressure phases of solid ZnX, CdX, and HgX (X = S, Se, and Te): trends and relativistic effects.,” *The Journal of chemical physics*, vol. 137, no. 3, p. 034705, Jul. 2012.

[40] W. Demtroder, *Atoms, Molecules and Photons*. New York: Springer, Berlin, Heidelberg, 2006.

[41] R. Car and M. Parrinello, “Unified approach for molecular dynamics and density-functional theory,” *Physical Review Letters*, vol. 55, no. 22, p. 2471, 1985.

[42] P. Pulay, “Convergence acceleration of iterative sequences. The case of SCF iteration,” *Chemical Physics Letters*, vol. 73, no. 2, p. 393, 1980.

[43] H. J. Monkhorst and J. D. Pack, “Special points for Brillouin-zone integrations,” *Physical Review B*, vol. 13, no. 12, pp. 5188–5192, 1976.

[44] O. Madelung, *Semiconductors: data handbook*, 3rd ed. Springer, Berlin, Heidelberg, 2004.

[45] S. V Streltsov, a Y. Manakov, a P. Vokhmyanin, S. V Ovsyannikov, and V. V Shchennikov, "Crystal lattice and band structure of the intermediate high-pressure phase of PbSe.," *Journal of Physics. Condensed Matter* , vol. 21, no. 38, p. 385501, Sep. 2009.

[46] F. Murnaghan, "The compressibility of media under extreme pressures," *Proceedings of the National Academy of Sciences*, vol. 30, pp. 244–247, 1944.

[47] F. Birch, "Finite elastic strain of cubic crystals," *Physical Review*, vol. 71, no. 11, p. 809, 1947.

[48] K. Parlinski and Y. Kawazoe, "Ab initio study of phonons and structural stabilities of the perovskite-type MgSiO3," *The European Physical Journal B*, vol. 58, no. 16, pp. 49–58, 2000.

[49] H. W. Leite Alves, a. R. R. Neto, L. M. R. Scolfaro, T. H. Myers, and P. D. Borges, "Lattice contribution to the high dielectric constant of PbTe," *Physical Review B*, vol. 87, no. 11, p. 115204, Mar. 2013.

[50] C. C. Silva, H. W. Leite Alves, L. M. R. Scolfaro, and J. R. Leite, "Pressure-induced phase transitions and polytypic structures in III-Nitrides," *Physica Status Solidi (C)*, vol. 2, no. 7, pp. 2468–2471, May 2005.

[51] K. Kunc and R. Martin, "Ab initio force constants of GaAs: A new approach to calculation of phonons and dielectric properties," *Physical Review Letters*, vol. 48, no. 6, pp. 406–409, 1982.

[52] M. A. Blanco, E. Francisco, and V. Luaña, "GIBBS: isothermal-isobaric thermodynamics of solids from energy curves using a quasi-harmonic Debye model," *Computer Physics Communications*, vol. 158, no. 1, pp. 57–72, Mar. 2004.

[53] T. Grandke, L. Ley, and M. Cardona, "Angle-resolved uv photoemission and electronic band structures of the lead chalcogenides," *Physical Review B*, vol. 18, no. 8, p. 3847, 1978.

[54] V. Hinkel, H. Haak, C. Mariani, and L. Sorba, "Investigation of the bulk band structure of IV-VI compound semiconductors: PbSe and PbTe," *Physical Review B*, vol. 40, no. 8, p. 5549, 1989.

[55] a. Svane, N. Christensen, M. Cardona, A. Chantis, M. Van Schilfgaarde, and T. Kotani, "Quasiparticle self-consistent GW calculations for PbS, PbSe, and PbTe: Band structure and pressure coefficients," *Physical Review B*, vol. 81, no. 24, pp. 1–10, Jun. 2010.

[56] L. Xu, H.-Q. Wang, and J.-C. Zheng, "Thermoelectric Properties of PbTe, SnTe, and GeTe at High Pressure: an Ab Initio Study," *Journal of Electronic Materials*, vol. 40, no. 5, pp. 641–647, Jan. 2011.

[57] F. Kong, Y. Liu, B. Wang, Y. Wang, and L. Wang, “Lattice dynamics of PbTe polymorphs from first principles,” *Computational Materials Science*, vol. 56, pp. 18–24, Apr. 2012.

[58] A. Crocker and M. Wilson, “Microhardness in PbTe and related alloys,” *Journal of Materials Science*, vol. 13, pp. 833–842, 1978.

[59] Y. Gelbstein, G. Gotesman, Y. Lishzinker, Z. Dashevsky, and M. P. Dariel, “Mechanical properties of PbTe-based thermoelectric semiconductors,” *Scripta Materialia*, vol. 58, no. 4, pp. 251–254, Feb. 2008.

[60] J. E. Ni, E. D. Case, K. N. Khabir, R. C. Stewart, C.-I. Wu, T. P. Hogan, E. J. Timm, S. N. Girard, and M. G. Kanatzidis, “Room temperature Young’s modulus, shear modulus, Poisson's ratio and hardness of PbTe–PbS thermoelectric materials,” *Materials Science and Engineering: B*, vol. 170, no. 1–3, pp. 58–66, Jun. 2010.

[61] Y. Gelbstein, Z. Dashevsky, and M. P. Dariel, “The search for mechanically stable PbTe based thermoelectric materials,” *Journal of Applied Physics*, vol. 104, no. 3, p. 033702, 2008.

[62] Y. Gelbstein, Z. Dashevsky, and M. P. Dariel, “In doped $Pb_{0.5}Sn_{0.5}Te$ p-type samples prepared by powder metallurgical processing for thermoelectric applications,” *Physica B: Condensed Matter*, vol. 396, no. 1–2, pp. 16–21, Jun. 2007.

[63] Y. Gelbstein, Z. Dashevsky, and M. P. Dariel, “Powder metallurgical processing of functionally graded $Pb_{1-x}Sn_xTe$ materials for thermoelectric applications,” *Physica B: Condensed Matter*, vol. 391, no. 2, pp. 256–265, Apr. 2007.

[64] G. T. Alekseeva, M. V Vedernikov, and E. A. Gurieva, “Hole Concentration and Thermoelectric Figure of Merit for $Pb_{1-x}Sn_xTe$: Te Solid Solutions,” *Semiconductors*, vol. 34, no. 8, pp. 935–939, 2000.

[65] M. Orihashi, Y. Noda, C. LIDONG, and T. Hirai, “Carrier concentration dependence of thermal conductivity of iodine-doped n-type PbTe,” *Materials transactions-JIM*, vol. 41, no. 10, p. 1282, 2000.

[66] D. V. Talapin, C. T. Black, C. R. Kagan, E. V. Shevchenko, a. Afzali, and C. B. Murray, “Alignment, Electronic Properties, Doping, and On-Chip Growth of Colloidal PbSe Nanowires,” *Journal of Physical Chemistry C*, vol. 111, no. 35, pp. 13244–13249, Sep. 2007.

[67] R. Hill, “The elastic behaviour of a crystalline aggregate,” *Proceedings of the Physical Society. Section A*, vol. 65, p. 349, 1952.

[68] S. Pugh, “XCII. Relations between the elastic moduli and the plastic properties of polycrystalline pure metals,” *Philosophical Magazine*, vol. 45, no. 367, pp. 823–843, 1954.

[69] F. Nye, *Physical properties of crystals*, 2nd ed. Oxford: Oxford University Press, 1964.

[70] S. Aydin, Y. O. Ciftci, and A. Tatar, “Superhard transition metal tetranitrides: XN4 (X = Re, Os, W),” *Journal of Materials Research*, vol. 27, no. 13, pp. 1705–1715, May 2012.

[71] M. A. Caravaca, J. C. Miño, V. J. Pérez, R. a Casali, and C. A. Ponce, “Ab initio study of the elastic properties of single and polycrystal TiO(2), ZrO(2) and HfO(2) in the cotunnite structure.,” *Journal of physics. Condensed matter : an Institute of Physics journal*, vol. 21, no. 1, p. 015501, Jan. 2009.

VITA

John E. Petersen III was born in Webster, TX on June 25, 1981, the son of John E. Petersen Jr. and Joanna E. Petersen. His father introduced him to science at a young age, and this would stay with him the rest of his life. While studying international culture and business in his early 20's, he studied abroad in Germany and Spain, and he received his B.A. from The University of Texas at Austin in 2005. After working as a financial advisor for a couple of years, he decided to go back to school in 2008 to pursue his passion for physics, and he graduated from The University of Texas at San Antonio in 2010 with a B.S. in physics. He entered the Graduate College of Texas State University–San Marcos in the fall of 2011.

Permanent Email Address: jepeterseniii@yahoo.com

This thesis was typed by John E. Petersen III.